Reconciling Ground-Based and Space-Based Estimates of the Frequency of Occurrence and Radiative Effect of Clouds around Darwin, Australia

A. PROTAT,* S. A. YOUNG,* S. A. MCFARLANE,+ T. L'ECUYER,# G. G. MACE,@ J. M. COMSTOCK,+ C. N. LONG,+ E. BERRY,@ AND J. DELANOË&

* *Centre for Australian Weather and Climate Research, Melbourne, Australia*
+ *Pacific Northwest National Laboratory, Richland, Washington*
# *University of Wisconsin—Madison, Madison, Wisconsin*
@ *University of Utah, Salt Lake City, Utah*
& *Laboratoire Atmosphère, Milieux, Observations Spatiales, Guyancourt, France*

(Manuscript received 25 February 2013, in final form 19 August 2013)

ABSTRACT

The objective of this paper is to investigate whether estimates of the cloud frequency of occurrence and associated cloud radiative forcing as derived from ground-based and satellite active remote sensing and radiative transfer calculations can be reconciled over a well-instrumented active remote sensing site located in Darwin, Australia, despite the very different viewing geometry and instrument characteristics. It is found that the ground-based radar–lidar combination at Darwin does not detect most of the cirrus clouds above 10 km (because of limited lidar detection capability and signal obscuration by low-level clouds) and that the *CloudSat* radar–Cloud–Aerosol Lidar with Orthogonal Polarization (CALIOP) combination underreports the hydrometeor frequency of occurrence below 2-km height because of instrument limitations at these heights. The radiative impact associated with these differences in cloud frequency of occurrence is large on the surface downwelling shortwave fluxes (ground and satellite) and the top-of-atmosphere upwelling shortwave and longwave fluxes (ground). Good agreement is found for other radiative fluxes. Large differences in radiative heating rate as derived from ground and satellite radar–lidar instruments and radiative transfer calculations are also found above 10 km (up to 0.35 K day^{-1} for the shortwave and 0.8 K day^{-1} for the longwave). Given that the ground-based and satellite estimates of cloud frequency of occurrence and radiative impact cannot be fully reconciled over Darwin, caution should be exercised when evaluating the representation of clouds and cloud–radiation interactions in large-scale models, and limitations of each set of instrumentation should be considered when interpreting model–observation differences.

1. Introduction

The interactions between clouds and radiation have a major impact on weather and climate. As a result, these interactions need to be reproduced accurately in large-scale models for numerical weather prediction and climate projections (e.g., Solomon et al. 2007). The A-Train constellation of satellites (L'Ecuyer and Jiang 2010; Stephens et al. 2002) allows for a unique and comprehensive examination of clouds, precipitation, aerosols, and their influences on the longwave and shortwave radiation streams. The unique synergy of the A-Train constellation is due to the broad diversity of instrumentation that includes the active remote sensors *Cloud–Aerosol Lidar and Infrared Pathfinder Satellite Observations* (*CALIPSO*; Winker et al. 2009), including the Cloud–Aerosol Lidar with Orthogonal Polarization (CALIOP), and the first cloud-sensing millimeter-wave radar in space (*CloudSat*; Im et al. 2006). The active remote sensors are complemented by passive measurements that span the electromagnetic spectrum and include the Moderate Resolution Imaging Spectroradiometer (MODIS; Platnick et al. 2003), the Clouds and the Earth's Radiant Energy System (CERES; Wielicki et al. 1998), and the Advanced Microwave Scanning Radiometer for Earth Observing System (AMSR-E; Wentz and Meissner 2000). The principal limitations of the A-Train mission, relative to suites of ground-based remote sensors, are the sparse sampling of the diurnal cycle (two

Corresponding author address: Alain Protat, Centre for Australian Weather and Climate Research (CAWCR), 700 Collins Street, Docklands, Melbourne VIC3008, Australia.
E-mail: a.protat@bom.gov.au

DOI: 10.1175/JAMC-D-13-072.1

sun-synchronous overpasses of any region per day) and the limited capabilities inherent to the deployment of instruments in space (i.e., a radar blind zone between the surface and 1 km, cloud radar sensitivity of approximately −30 dBZ, no Doppler velocity information, reduced lidar signal-to-noise ratio during daytime, etc.). These limitations are ameliorated by the global nature of the measurements. Ground-based remote sensing sites like those deployed around the world by the U.S. Department of Energy Atmospheric Radiation Measurement (ARM) Program (Ackerman and Stokes 2003) or the European Union CloudNet project (Illingworth et al. 2007) complement the A-Train satellite observations by being able to concentrate a suite of state-of-the-art instrumentation in a single location. Indeed, the ground-based combination of cloud radars, lidars, microwave radiometers, and ground-based radiation measurements, complemented by radiative transfer calculations (e.g., Mather et al. 2007; McFarlane et al. 2008), characterizes the physical properties of the full diurnal cycle of cloud, aerosol, and radiative properties. Such clustering of instrumentation in a single location results in highly detailed local descriptions, which may, however, not be relevant to even regional statistics.

Our understanding of the A-Train data streams has now reached a high level of maturity since the launch of *CloudSat* and *CALIPSO* in 2006. Increasingly sophisticated official and experimental products characterizing cloud, aerosol, precipitation, and radiative properties are now available for quantitative evaluation by the scientific community. Similarly, long time series of geophysical properties are now available from a number of ground-based sites. The main purpose of this paper is to investigate whether, despite obvious differences in viewing geometry and instrumental characteristics, estimates of the frequency of occurrence of hydrometeors and associated cloud radiative forcing as derived from ground-based and satellite active remote sensing and radiative transfer calculations can be reconciled. Thorsen et al. (2011) have done such comparisons between ground-based ARM lidar data in the tropics and *CALIPSO*, demonstrating cirrus detection issues with the ARM ground-based lidars. In our study, we complement that study by using cloud radar and lidar data together, and we assess the radiative impact of these cloud detection issues. Also, additional measurements of surface and top-of-atmosphere (TOA) radiation are used to assess whether any of these products can be used with confidence. It is necessary to clearly understand the strengths and limitations of each observational paradigm so that case study and long-term statistical studies, as well as the evaluation of numerical weather prediction and climate models, can be undertaken with confidence.

As cloud microphysical radar–lidar retrievals (Protat et al. 2010a,b, 2011) and radiative transfer calculations (Comstock et al. 2013) had already been carried out for a long period of time (2005–09) over the Darwin, Australia, ARM site, this study focuses on statistical comparisons over this site. The paper is organized as follows. The large number of observations and products used and the strategy employed to compare ground-based and satellite products are described in section 2. The comparisons of hydrometeor frequencies of occurrence and retrieved cloud microphysics are presented in section 3. The impacts of the differences obtained in section 3 are then characterized in terms of radiative effect differences at the surface and the top of the atmosphere (section 4) and of radiative heating-rate profile differences (section 5). Concluding remarks are given in section 6.

2. Observations and methodology

In this paper, 2 yr (2007 and 2008) of ARM ground-based and *CloudSat–CALIPSO* cloud frequencies of occurrence and radiative fluxes are compared. In what follows, we briefly describe each product used, as well as the strategy adopted for the ground–satellite comparisons.

a. Ground-based ARM cloud mask and radiative fluxes

The primary ARM instruments used in this study are the ARM Millimeter Wave Cloud Radar (MMCR; Moran et al. 1998), which operates at 35 GHz, and the micropulse lidar (MPL; Campbell et al. 2002), which operates at 532 nm. Our input files include the CloudNet-processed MMCR dataset (Illingworth et al. 2007), the ARM-produced Merged Sounding value-added product for thermodynamic profiles (Troyan 2010), and MPL backscatter profiles (details about the CloudNet- and ARM-processed datasets can be obtained online at http://www.cloud-net.org and http://www.arm.gov, respectively). Each measurement was averaged over 2 min temporally and 300 m vertically. From these individual inputs, a common cloud mask was produced using both radar and lidar cloud detections. This ground-based cloud mask product has already been used to evaluate the calibration of the *CloudSat* radar (Protat et al. 2009) and the *CloudSat*-only microphysical products (Protat et al. 2010a) to characterize the variability of tropical ice cloud properties as a function of the large-scale context (Protat et al. 2011) and to carry out ice microphysical retrieval technique intercomparisons (Comstock et al. 2013). The profiles are separated into nonprecipitating cloud profiles and precipitating cloud profiles [the principle is explained in Protat et al. (2009, 2010a)], which will be referred to as ''cloud'' and

''convection'' profiles in the following. The two reasons for doing this are that (i) the different geometry of observations (from ground up or from top down) induces large differences in convective profiles (less in cloud profiles) and (ii) microphysical retrievals for ground-based and spaceborne convective profiles are not mature enough to be trusted, mainly because of different paths for attenuation in both measurements and multiple scattering effects in the *CloudSat* beam (e.g., Battaglia et al. 2008; Matrosov et al. 2008; Bouniol et al. 2008).

The ARM retrieval algorithm retrieves liquid cloud microphysical properties by relating the radar reflectivity Z_e to the liquid water content (LWC) such that $\mathrm{LWC} = (N_d/3.6 \times Z)^{1/1.8}$, where N_d is the drop number concentration and is assumed to be $100\,\mathrm{cm}^{-3}$ (Liao and Sassen 1994). The effective radius r_e is computed using a lognormal droplet distribution that is scaled according to the derived LWC (Frisch et al. 1995). For liquid clouds when only lidar detects cloud, we assume $r_e = 5.0\,\mu\mathrm{m}$ and apply the parameterization of Slingo (1989) at the lidar wavelength, which relates the visible extinction coefficient to the r_e and LWC.

The ice cloud microphysical properties are derived using the VarCloud variational radar–lidar retrieval technique (Delanoë and Hogan 2008). This algorithm retrieves ice cloud properties seamlessly between regions of the cloud detected by both radar and lidar and regions detected by just one of these two instruments. More details about the technique can be found in Delanoë and Hogan (2008), and a comprehensive summary is available in Comstock et al. (2013). These microphysical properties are then used as inputs to the Fu–Liou four-stream radiative transfer (RT) model (Fu and Liou 1992; Fu 1996) in order to compute shortwave (SW) and longwave (LW) fluxes. These will be referred to as the ARM RT radiative fluxes throughout this paper.

At the surface (SFC throughout this paper), we use as a reference the ARM Radiative Flux Analysis product (hereafter referred to as RADFLUX), which includes the best estimates of the downwelling and upwelling SW and LW all-sky hemispheric fluxes from the ARM ''surface radiation quality testing methodology'' (''QCRad'') value-added product (Long and Shi 2006, 2008). Estimates of random (2 sigma) uncertainties of the 1-min flux measurements are of about $10\,\mathrm{W\,m}^{-2}$ for the downwelling SW fluxes and $4\,\mathrm{W\,m}^{-2}$ for the downwelling LW fluxes (Table 1 in McFarlane et al. 2013). More details about the radiation systems and instruments used at the ARM site can also be found in McFarlane et al. (2013).

b. Satellite-derived cloud mask and radiative fluxes

The *CloudSat–CALIPSO* cloud mask used in this study is the official 2B-GEOPROF-lidar product (Mace et al. 2007, 2009; Marchand et al. 2008). The European Centre for Medium-Range Weather Forecasts (ECMWF) auxiliary product (Partain 2004) is also used. The ECMWF auxiliary product provides ECMWF state variable data that have been interpolated to each radar bin. The ECMWF temperatures are used to locate the 0°C isotherm altitude and separate cloud and convection profiles, as discussed in the previous section.

Three radiative flux products are used in the comparisons with ground-based radiative fluxes, which are derived at the resolution of the *CloudSat* measurements (about $1.4\,\mathrm{km} \times 1.7\,\mathrm{km}$; Tanelli et al. 2008). The two first radiative flux products used are the official *CloudSat*-only level-2B Fluxes and Heating Rates product (2B-FLXHR; L'Ecuyer et al. 2008) and the *CloudSat–CALIPSO* 2B-FLXHR-lidar (Henderson et al. 2013). Both products use the same RT model (L'Ecuyer et al. 2008) and the level-2B Radar–Visible Optical Depth Cloud Water Content (2B-CWC-RVOD) microphysical retrieval (Austin et al. 2009; Benedetti et al. 2003). However, the 2B-FLXHR-lidar product includes additional *CALIPSO* and MODIS microphysical properties of cloud and aerosol bins undetected by *CloudSat*, following a complex procedure described in Henderson et al. (2013). The third radiative flux product is the experimental 2C-ICE-FLUX product. Cloud microphysical and radiative properties are derived using a suite of techniques that is described in Mace (2010). The ice microphysical properties are obtained from the official 2C-ICE *CloudSat* data product (Deng et al. 2010, 2013). The 2C-ICE algorithm uses *CloudSat* radar reflectivity factor and *CALIPSO* attenuated backscattering coefficients as inputs in an optimal estimation framework to retrieve profiles of ice microphysics. We use the radar reflectivity factor, the MODIS visible optical depths from the MODIS level-2 Joint Atmosphere Product (Platnick et al. 2003), and liquid water paths derived from AMSR-E microwave brightness temperatures (Wentz and Meissner 2000) in the retrieval of liquid cloud properties (see appendix A of Mace 2010). For liquid water, we use the Slingo (1989) and Kiehl et al. (1998) parameterizations for the shortwave and longwave radiative properties, respectively. For ice, we use the Fu (1996) and Fu et al. (1998) parameterization for the shortwave and longwave radiative properties, respectively. We use the two-stream radiative transfer model described by Toon et al. (1989) with the k distribution method and correlated-k assumption described by Kato et al. (1999, 2001) for the solar spectrum and by Mlawer et al. (1997) for the infrared spectrum.

At TOA, the CERES Fast Longwave and Shortwave Flux (FLASHFlux) upwelling fluxes at TOA are used as the reference. These fluxes are available at a

20 km × 20 km pixel resolution. CERES algorithms convert a directional measurement to a hemispheric flux using angular directional models that depend on cloud properties and surface type. For all-sky conditions, Loeb et al. (2007) estimated instantaneous TOA flux errors due to angular direction model assumptions of about 10 W m^2 in the SW and 3–5 W m^{-2} in the LW. The overall bias in regional monthly mean SW TOA flux is less than 0.2 W m^{-2}, and the regional root-mean-square error ranges from 0.70 to 1.4 W m^{-2}. In the LW, the bias error ranges from 0.2 to 0.4 W m^{-2}, and the regional root-mean-square errors remain smaller than 0.7 W m^{-2}.

c. Comparison methodology

To compare ground-based and spaceborne observations, we have considered *CloudSat–CALIPSO* data within a radius of 200 km around the ground-based site and ±1 h around the satellite overpass of that area. Sensitivity studies presented in Protat et al. (2009) indeed indicated with the same dataset that these numbers provided a good trade-off between the need for a large statistical sample and the invariance of cloud properties over the spatial and temporal intervals considered. The total number of profiles obtained using this procedure over 2 yr is 1.6×10^5 for the satellite observations and 4.5×10^6 for the ground-based observations.

These comparisons are by construction affected by the different geometry of observations. This has particularly important implications for the comparison of ground-based and spaceborne ice cloud observations. Indeed, most ice cloud observations from space will be reasonably unattenuated (except in some mixed-phase clouds). In contrast, a significant portion of the ice cloud observations using radar–lidar from ground will be attenuated by any liquid cloud below ice clouds or by the liquid part of the deep convective systems to which they belong. It is an important objective of this study to assess the importance of the viewing geometry differences on the cloud radiative properties, so we do not attempt to screen out these problematic cases but rather choose deliberately to include them.

Our initial aim in section 4 was to compare cloud radiative effects (also referred to as ''cloud radiative forcing'' in the literature) obtained from the satellite and ground-based, vertically pointing radar–lidar observations and from the ''reference'' hemispheric flux measurements at SFC and TOA. However, when analyzing these results, several problems were noted and mitigated as follows.

- The derivation of cloud radiative effect from the reference hemispheric measurements is achieved at the expense of more assumptions and errors than if fluxes are directly compared. Therefore, we compare SFC and TOA fluxes instead of cloud radiative forcing.
- The proportion of clear-air cases (inducing zero cloud radiative effect) in the reference measurements was about half that of the satellite and ground-based estimates from vertically pointing radar–lidar observations (due to hemispheric versus ''vertical pencil beam'' views of the same cloud scene). Therefore, in our comparison, the ground-based and satellite clear-sky profiles are excluded individually.
- Initially, in order to mitigate the potential effect of partial hemispheric cloud filling (cloud fractions lower than 1), we implemented a test to retain only scenes with cloud fractions greater than 0.9. Only 471 points for the SW and 855 points for the LW were included in the analysis with that test, resulting in very noisy flux probability distribution functions (PDFs; not shown). The correlation coefficient between CERES fluxes and the two satellite estimates was for that test 0.90–0.91 for the SW and 0.96 for the LW. In comparison, when including all cloud scenes, 2027 points for the SW and 3568 points for the LW are included in the analysis, and the correlation coefficients with the CERES fluxes are not degraded (0.88–0.90 for the SW and 0.95 for the LW). Therefore, we have included all cloud scenes in the analysis.
- The RADFLUX product shows occurrences of positive SW cloud radiative forcing. The occurrence of SW amounts greater than the equivalent clear-sky amounts is a common occurrence for any particular location at the surface and is caused by the increased downward scattering of clouds (over the equivalent clear-sky amount) from any area of the sky where clouds reside, while at the same time the direct sun is not blocked by cloud (Long and Ackerman 2000; Long and McFarlane 2012). These positive SW cloud radiative effects are real, but they correspond to processes that are not permitted in plane-parallel RT calculations using vertical beam geometry. To mitigate that effect, when this situation was encountered on a given RADFLUX measurement, this time was removed from all statistics computed.
- The surface conditions (albedo) at the ARM site do change as a function of solar zenith angle in clear-sky periods (Long 2008; May et al. 2012). The surface albedo is assumed to be constant (0.095) in the ARM RT calculations while the satellite calculations use surface albedos obtained from seasonally varying maps of surface reflectance properties. In the 2B-FLXHR-lidar product, there are 50% surface albedos values of 0.07, 45% values of 0.09, and very small occurrences

of values around 0.12 and 0.18. To mitigate possible differences due to this effect at least on the SFC comparisons, only the *downwelling* SFC fluxes are compared. However, these differences will contribute to the TOA differences and to an extent that will be investigated later in this paper on the downwelling SFC fluxes through multiple-reflection effects.

- Differences of 3–4 $W m^{-2}$ were also found between the different datasets for the downwelling TOA fluxes. Therefore, in what follows, we have chosen to compare only the *upwelling* TOA fluxes.
- Some radiative flux products include the effect of aerosols (e.g., 2B-FLXHR-lidar) and some do not (e.g., the ground-based calculations). This potential source of differences has been quantified by comparing the two versions of the 2B-FLXHR-lidar product with and without including the aerosols in the calculations in all-sky conditions and by comparing the 2B-FLXHR-lidar product (which includes aerosols) and the 2C-ICE product (which does not) in clear-air situations. In those two comparisons, it is found that the functional form of the flux PDFs are virtually unaltered; the statistical differences found between median fluxes were less than 4 $W m^{-2}$ for SW fluxes and less than 1 $W m^{-2}$ for LW fluxes at both SFC and TOA, and they were certainly negligible when compared with the differences discussed in what follows.
- The differences between clear-air downwelling SFC and upwelling TOA fluxes at ground and TOA is another potential source of differences that cannot be attributed to clouds. These differences have been investigated separately using the clear-air profiles. At SFC, it is found that the satellite product agrees to within 1 $W m^{-2}$ and that the downwelling SW (LW) ARM RT clear-air fluxes are 5.5 $W m^{-2}$ larger (2 $W m^{-2}$ smaller) than the 2B-FLXHR-lidar and 2C-ICE clear-air SW (LW) fluxes. At TOA, the satellite products again agree to within 1 $W m^{-2}$, while the upwelling SW (LW) ARM RT clear-air fluxes are 6 $W m^{-2}$ (4 $W m^{-2}$) larger than the 2B-FLXHR-lidar and 2C-ICE clear-air SW (LW) fluxes. This information will be used in section 4 to discuss the respective roles of clear-air and cloudy scenes in the observed all-sky flux differences.

Despite these limitations, and with the actions taken to mitigate these effects, we assume in what follows that errors associated with the very indirect nature of ground-based and satellite estimates of the radiative fluxes (RT model assumptions about cloud optical properties and radar–lidar microphysical retrievals) are much larger than the errors due to the differences discussed previously.

3. Comparison of cloud frequency of occurrence and microphysics

Consistency between ground-based and satellite estimates of the hydrometeor frequency of occurrence measurements is presumably essential to produce consistent estimates of the interactions between hydrometeors and incoming and outgoing radiation. Microphysical properties such as optical depth and effective radius are also crucial in that respect; however, the presence or absence of clouds at a particular atmospheric level and at a particular time is the primary determinant of the radiation perturbations. The satellite and ground-based estimates of the all hydrometeors frequency of occurrence (HFO), which is defined as the number of times a radar–lidar vertical (height) range bin (referred to as radar or lidar bin in the following) contains hydrometeors divided by the number of times the bin is sampled (where the bins here are vertical slabs 500 m thick), are compared in Fig. 1a. All hydrometeors means anything detected by the radar and/or the lidar that is not clear air, nonmeteorological targets, or aerosols. The all hydrometeors profiles are then further subdivided into ''cloud'' profiles (profiles characterized by no precipitation detected at ground; Fig. 1b) and ''convection'' profiles (profiles characterized by precipitation detected at ground; Fig. 1c).

Going back to Fig. 1, two main features can be clearly observed. The first feature is an underreporting of the HFO below 1.5 km height by *CloudSat–CALIPSO*. The principal reason for this underreporting is the contamination of the first two or three *CloudSat* radar bins above the earth's surface by radar ground clutter (and to some extent the attenuation and sometimes total extinction of the *CloudSat* beam in heavy precipitation and the extinction of the *CALIPSO* lidar beam by liquid clouds and precipitation). This underreporting is observed both for the cloud frequency of occurrence (CLFO; Fig. 1b) and the convective frequency of occurrence (COFO; Fig. 1c). The *CALIPSO* lidar does help increase the HFO and CLFO below 1.5-km height, but the improvement to the *CloudSat*-only frequency of occurrence remains moderate below 1.5 km. This bias appears to be smaller over ocean than over land, with a higher frequency of occurrence of hydrometeors detected over ocean than over land (Fig. 2b); thus, the land–ocean variability also plays a role in these differences.

The second main feature observed in Fig. 1 is the large underreporting of the HFO above 10-km height by the ground-based radar–lidar combination, which is mainly due to an underreporting of the CLFO (Fig. 1b), although this feature is also observed on the COFO profile (Fig. 1c). This large difference [which had also been

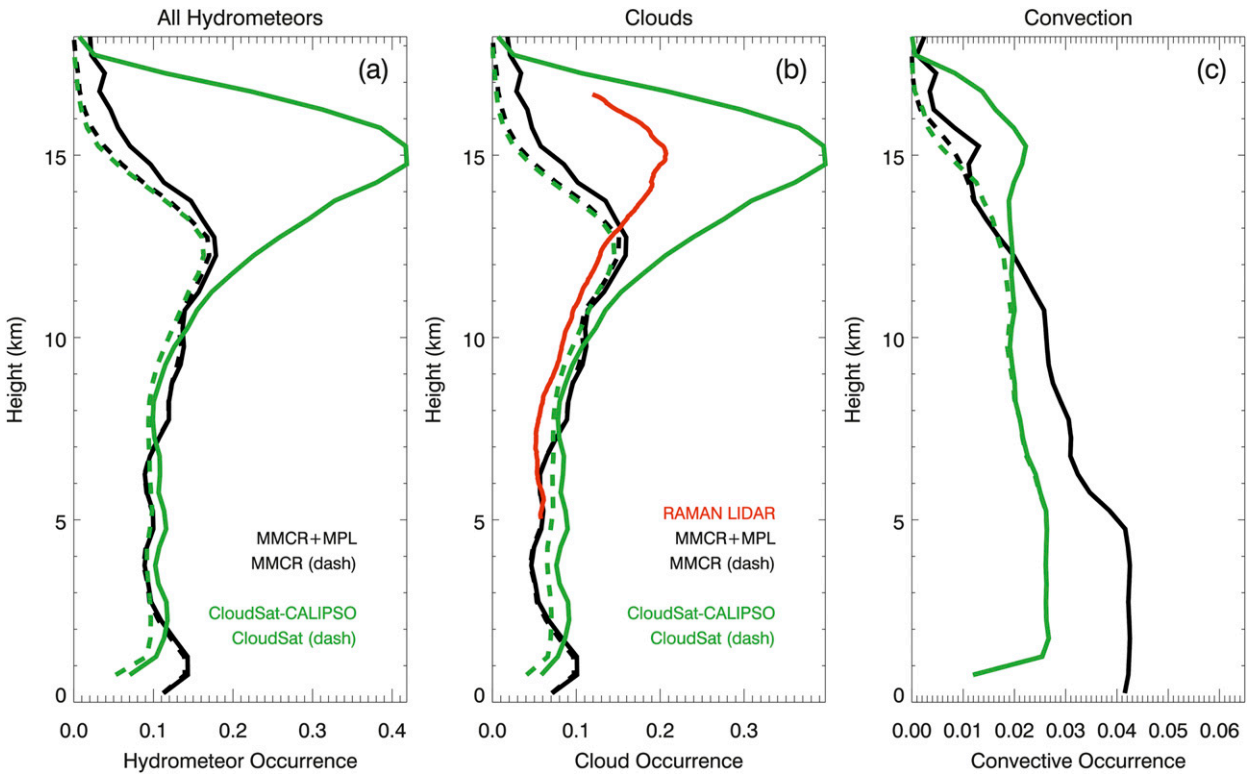

FIG. 1. Mean vertical profiles of the frequency of occurrence of (a) all hydrometeors, (b) clouds, and (c) convection. The black lines are the ground-based observations, and the green lines are the satellite-based observations (solid is radar–lidar and dashed is radar only). The red line in (b) is derived from Darwin Raman lidar observations.

found in Thorsen et al. (2011)] is expected to produce differences in the radiative fluxes and heating rates (investigated in sections 4 and 5). The ground-based HFO and CLFO peak at 13 km, with only a small contribution to the HFO and CLFO (on the order of 0.02–0.03) from the MPL lidar above 10 km. In contrast, it is above 10 km that the *CALIPSO* lidar detects more cirrus than the *CloudSat* radar, with a peak cirrus frequency of occurrence of 0.38 at 15-km height (Fig. 1b). The macrophysical, microphysical, and radiative properties of these clouds in the tropical belt have been extensively studied in Haladay and Stephens (2009), who reported that the typical cloud base of these clouds is higher than 10 km, their optical thickness ranges between 0.02 and 0.3, and their ice water path ranges between 0.5 and 4 $g\,m^{-2}$. The main tropics-wide cloud radiative effect is found to be a 4 $W\,m^{-2}$ LW heating. It must be noted, however, that they only considered cloud layers with lidar and at most two radar range bins, thereby excluding all upper parts of layers undetected by more than two *CloudSat* range bins, so they might have underestimated this effect.

As discussed above, unlike the space-based observations, the addition of the lidar in the ground-based observations does not significantly increase the HFO and CLFO above 10 km. This may be due to the geometry of the ground-based observations causing the MPL to be attenuated by lower clouds or may be due to the lower inherent sensitivity of the MPL compared to *CALIPSO* or some combination of both. To examine the role of attenuation by lower clouds, we calculated the ARM and *CloudSat–CALIPSO* frequency of occurrence of low, middle, and high cloud cover (clouds below 4.5 km, between 4.5 and 8 km, and above 8 km, respectively) as well as their frequency of overlap. All values are reported in Table 1. The *CloudSat–CALIPSO* high cloud cover (considered as the best estimate for the inferences made in the following) is 61.1%. It is to be noted that the ARM high cloud cover is only 43.3%, which again highlights, but from a layer-integrated perspective, the underreporting of high clouds by the ARM radar–lidar combination. The ARM low cloud cover is 24.4%, while the *CloudSat–CALIPSO* low cloud cover is actually slightly larger (27%) despite the underreporting found below 1.5 km. This result is actually probably due to the larger amount of liquid clouds detected by *CALIPSO* only in the 2–4.5-km layer (Fig. 1b). The frequency of overlap of low and high cloud cover derived

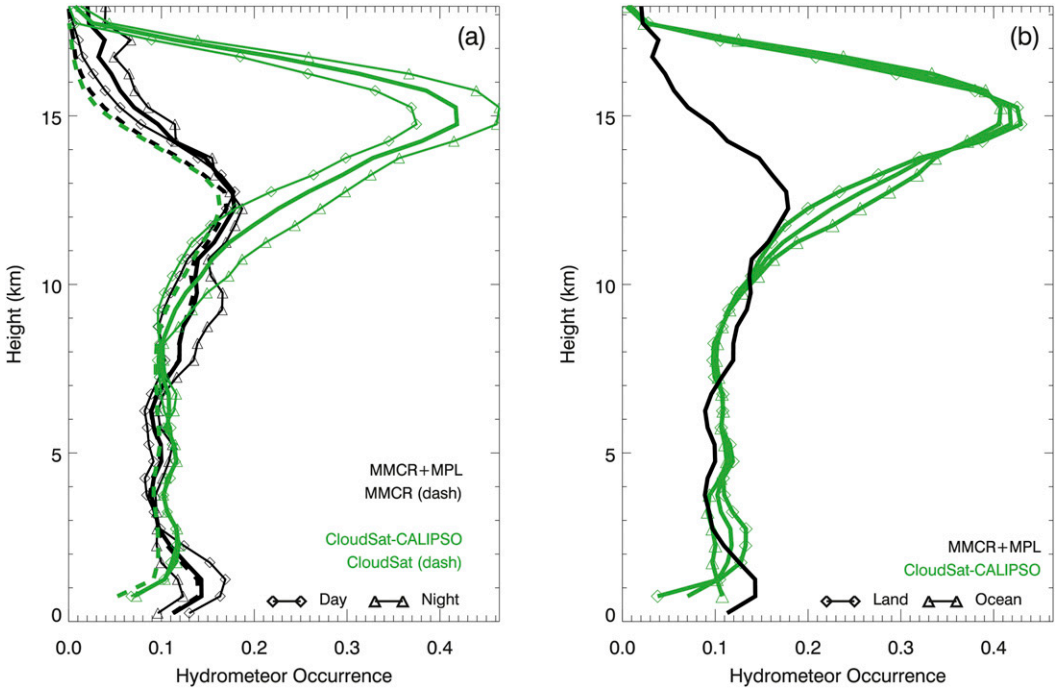

FIG. 2. (a) Day–night and (b) land–ocean variability of the mean vertical profile of hydrometeor frequency of occurrence. The black lines are the ground-based observations (the same for the two panels), and the green lines are the satellite-based observations [solid is radar–lidar; dashed is radar only; triangles are nighttime in (a) and land in (b); diamonds are daytime in (a) and ocean in (b)].

from *CloudSat–CALIPSO* is 19.8%, which can be considered as a lower bound given the underreported clouds below 1.5 km. If we assume that all low clouds fully attenuate the ground-based lidar signal and prevent detection of an upper cloud layer, then the effect of this obscuration would be an underestimation of CLFO by $0.198 \times 0.611 = 0.12$. Therefore, this low-level obscuration effect, although large, cannot explain solely the 0.30–0.35 differences between the ground-based and satellite CLFO observed at 15 km. This implies that the lower sensitivity of the MPL largely contributes to these differences. As the MPL sensitivity is better at night, we also examine differences between day and night ground-based and satellite observations (Fig. 2a). As expected, the MPL observes more cirrus at night, but so does *CloudSat–CALIPSO*, so the magnitude of the nighttime underreporting is actually similar to that during daytime.

The Darwin ARM site has also hosted a Raman lidar since December 2010. However, merged radar–lidar products using this Raman lidar are not available yet. To assess if this new lidar better detects the cirrus clouds underreported by the MPL, we processed the Raman lidar data at 2-min resolution for the December 2010 to April 2012 period and produced a mean vertical profile of CLFO from the Raman lidar alone (Fig. 1b). Although the mean vertical profile of CLFO derived from the Raman lidar alone still underreports CLFO above 10-km height, it is observed that the Raman lidar CLFO profile now peaks at the same height (15 km) as the *CloudSat–CALIPSO* profile. The Raman lidar detects 52% of the *CloudSat–CALIPSO* clouds at 15-km altitude, whereas MPL only detects 21% of these high clouds. In general, the detection of thin cirrus in the 13–17-km layer is dramatically improved with the Raman lidar when compared with the MPL. It is therefore recommended that the Raman lidar be used instead of the MPL for the estimate of the cloud radiative

TABLE 1. Frequency of occurrence (percent) of low-level ("low"; below 4.5 km), midlevel ("mid"; between 4.5 and 8 km), and high-level clouds ("high"; above 8 km) and of overlap between these cloud layers. These quantities are derived from the *CloudSat–CALIPSO* and ARM radar–lidar combinations separately.

	CloudSat–CALIPSO	ARM
Low cloud cover	27.0	24.4
Mid cloud cover	21.2	20.8
High cloud cover	61.1	43.3
Low + mid cloud cover	13.6	12.2
Mid + high cloud cover	18.5	16.7
Low + high cloud cover	19.8	15.2

effect using RT calculations and the ARM cloud microphysics retrievals (e.g., Mather et al. 2007; Comstock et al. 2013). Assuming that the MPLs at the other ARM sites have a similarly poor high-cloud detection performance, conclusions derived from previously published results should probably be revisited, especially the model evaluation studies. Some light is shed on this for the Darwin site in the next section, where the radiative impact of the underreported cirrus is investigated.

From Fig. 1b it is observed that the difference between the Darwin Raman lidar statistics and the *CloudSat–CALIPSO* statistics remains relatively large (about 0.18). As discussed previously from Table 1 results, the obscuration by low cloud cover would actually account for most of this difference in frequency of occurrence (a 0.12 effect on mean cloud frequency of occurrence at 15 km). Therefore, there is not much that can be done with a ground-based lidar system to improve this underreporting of cirrus given this obscuration effect. Fortunately, conditional sampling [for instance, excluding profiles where low-level obscuration occurs, as in Thorsen et al. (2011)] can be carefully designed for the sake of model and satellite product evaluation using data collected at the ground-based sites. The remaining differences between the Raman lidar and *CloudSat–CALIPSO* statistics at 15 km (about 0.06) might be due to the multiresolution detection technique used to detect weakly backscattering cloud and aerosol layers with CALIOP. Indeed, *CALIPSO*'s feature finder detects weakly backscattering features (cloud or aerosol layers) by averaging 1, 3, 15, 60, and 240 profiles (corresponding to horizontal resolutions of 0.33, 1, 5, 20, and 80 km, respectively) to improve signal-to-noise ratio (Vaughan et al. 2009; Winker et al. 2009). When a feature is detected at one horizontal-averaging resolution, the signal profile in which it was detected is truncated at the top of the feature before being used to create the average profile for the next, larger, horizontal resolution. This average profile is then also examined for features, which will have a smaller backscatter signal than those detected at the finer resolution, and the process continues up to the coarsest resolution. Although this approach has obvious advantages in terms of detection of increasingly tenuous features, the potential drawback is that if a feature can be detected in the averaged profile, it is mapped to the whole horizontal region averaged, which could artificially increase the apparent extent of clouds and bias the cloud distribution statistics, especially for broken cloud scenes. Figure 3 shows the vertical profile of the proportion of total *CALIPSO* cloud detection for each horizontal resolution. From this figure it is observed that at 15-km altitude 18% of clouds are detected at the 80-km resolution

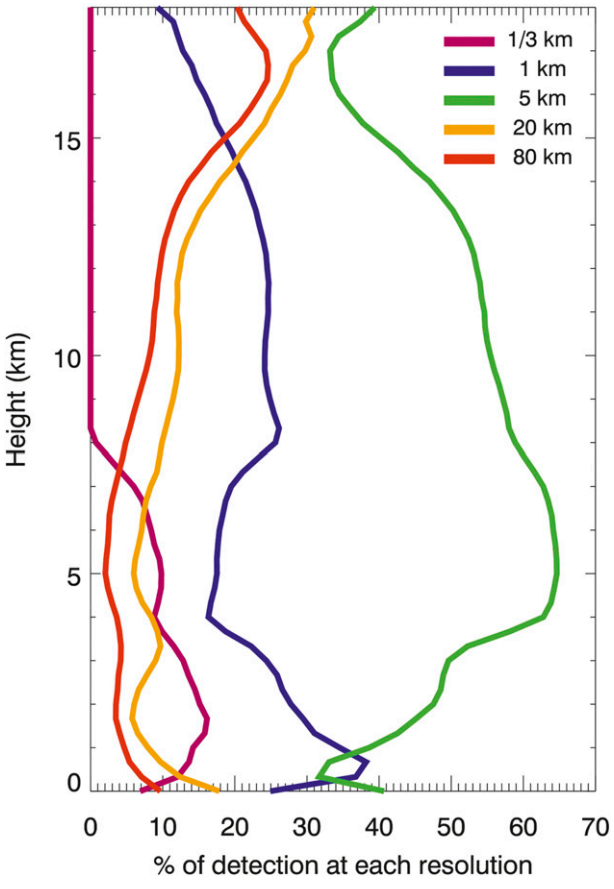

FIG. 3. Vertical profiles of the percentage of total cloud detection for the five horizontal resolutions used in the CALIOP feature-finder algorithm.

and 20% of clouds are detected at the 20-km resolution. If one assumes that the 2-min resolution of the MPL is equivalent to a 5-km-resolution measurement of the *CALIPSO* lidar (which would be exactly true for a 40 m s^{-1} wind at 15-km height), and one assumes a worst case in which, in all clouds detected at 80-km detection, fifteen of the sixteen 5-km cells forming the 80-km resolution and three of the four 5-km cells forming the 20-km detection are incorrectly filled (which is probably a large overestimation of the reality), then the corresponding overestimation in cloud frequency of occurrence would be $(15/16) \times 0.18 \times 0.40 + (3/4) \times 0.20 \times 0.40 = 0.127$ at 15-km height. Therefore, this potential *CALIPSO* overestimation can explain the remaining differences between the Raman lidar and *CloudSat–CALIPSO* statistics, but it cannot explain the differences between ground-based and satellite estimates of the CLFO when the MPL is used.

To characterize further the microphysical implications of the differences in cloud frequency of occurrence, the ground-based and satellite microphysical

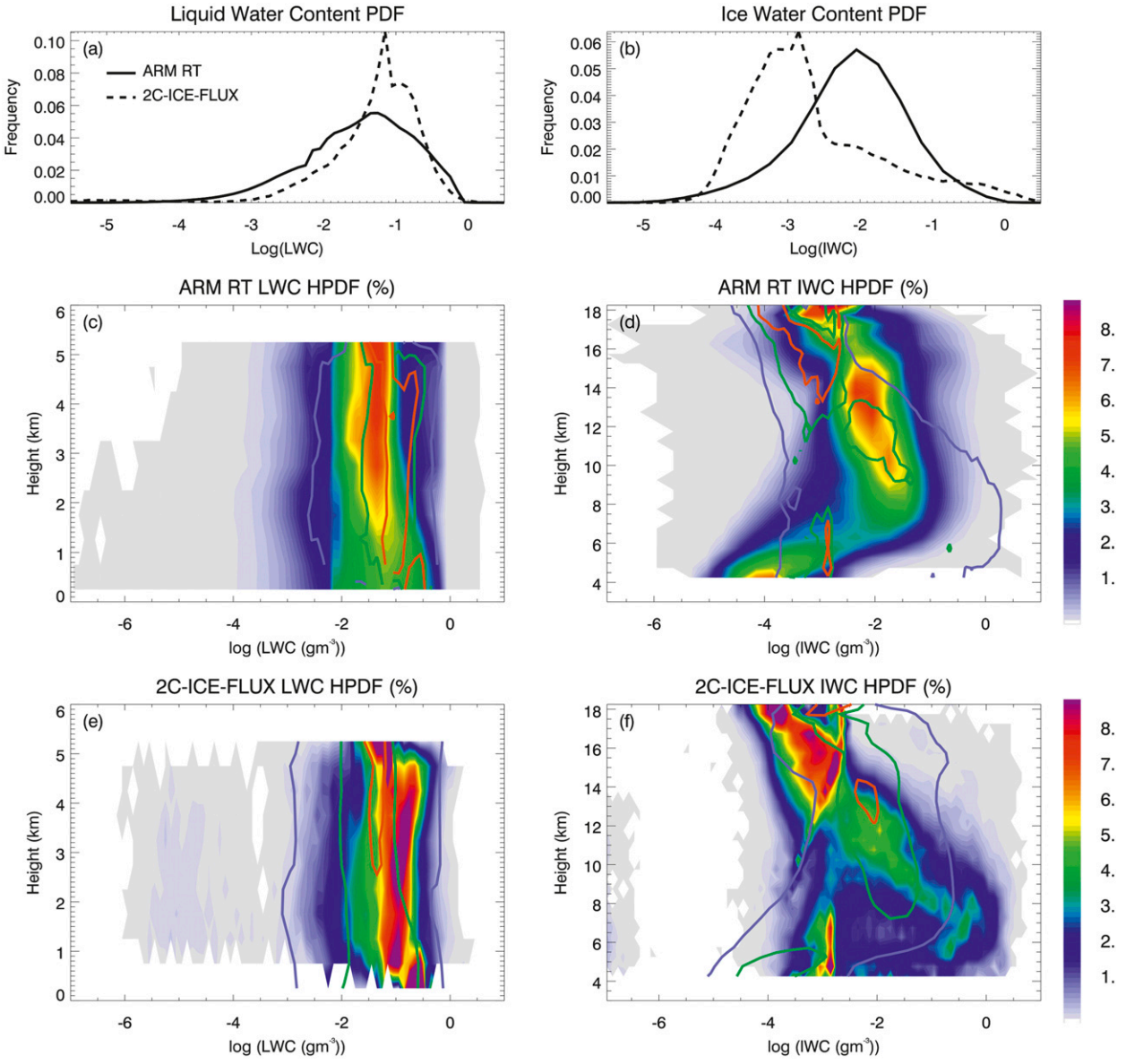

FIG. 4. Comparison of ground-based (ARM RT, solid) and satellite (2C-ICE-FLUX, dashed) PDFs of (a) LWC and (b) IWC. HPDFs of (c) ground-based LWC, (d) ground-based IWC, (e) satellite LWC, and (f) satellite IWC as given in colors. Selected contours at 1%, 4%, and 7% frequency of occurrence of the satellite HPDFs are also superimposed to the ground-based HPDFs, and vice versa, to facilitate comparisons.

retrievals are compared in Figs. 4 and 5, respectively, for water content and effective radius. Note that since multiple scattering is not corrected on the *CloudSat* signal, the errors on the precipitation profiles are expected to be much larger than for nonprecipitating clouds (see also discussion in section 2a). As a result, the convective clouds are excluded in these microphysical comparisons. The 2C-ICE-FLUX microphysics is used because the microphysical retrieval product used in 2B-FLXHR-lidar is not readily available, as it results from a complex merging of different microphysical products to include the *CALIPSO*-only cloud microphysics (Henderson et al. 2013). The PDFs of LWC (Fig. 4a), ice water content (IWC; Fig. 4b), liquid effective radius (Fig. 5a), and ice effective radius (Fig. 5b) are all found to be quite different, with the satellite PDF peaking at slightly higher LWC, larger liquid effective radii, lower ice effective radius, and much lower IWC (one order of magnitude). These differences can be further analyzed by looking at height-dependent PDFs

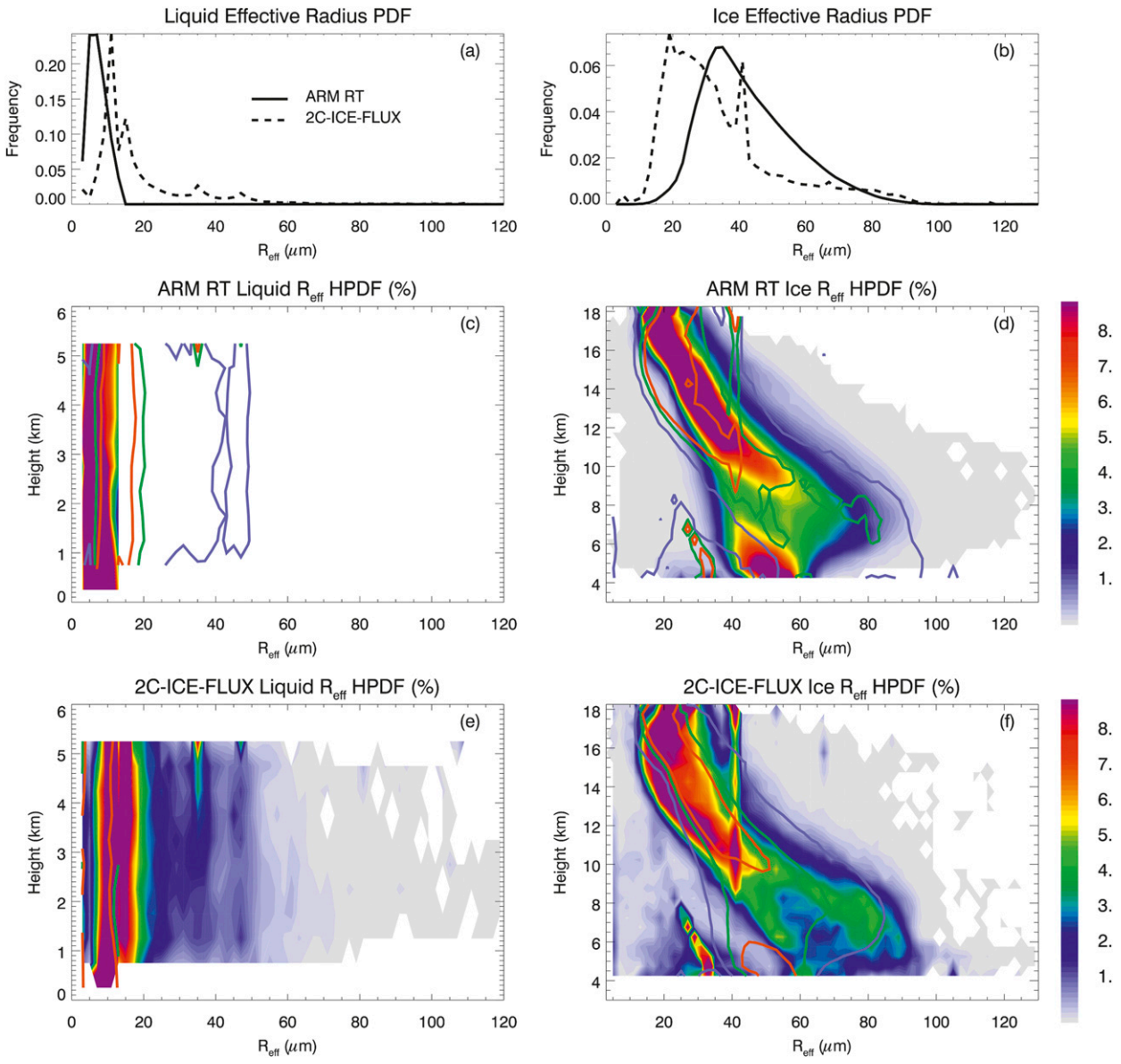

FIG. 5. As in Fig. 4, but replacing LWC with liquid effective radius and IWC with ice effective radius.

[HPDFs, which are PDFs in each height slab normalized by the total number of points in each height slab (Protat et al. 2009)]. From Figs. 4c and 4e, it is observed that the ground-based LWC peak value tends to decrease slightly with height, while the satellite LWC peak shows an opposite trend. The larger satellite-derived LWCs and liquid effective radii are found at all heights, and the satellite-derived PDF of liquid effective radius is also much broader at all heights. The differences in IWC HPDFs are more complex and much larger (Figs. 4d, 4f, 5d, 5f). The largest differences are found above 12 km and are clearly due to the underreporting of the thin cirrus at these heights (as seen in Fig. 1), which contribute as much larger occurrences of low IWC and low ice effective radii at these heights in the satellite HPDFs. The impact of these differences in CLFO and associated microphysical properties rates is characterized in terms of radiative fluxes and heating in the next two sections.

4. Comparison of ground-based and satellite radiative fluxes

Given the large differences in ground-based and satellite measurements of cloud frequency of occurrence and cloud microphysics documented in the previous

section, we aim to address two main questions in this section: 1) Do these differences correspond to large differences in cloud radiative forcing? 2) If the two estimates cannot be reconciled, what are the respective roles of cloud frequency of occurrence and cloud microphysics in those differences?

To better identify the potential radiative impact of the underreported low-level clouds by the satellite instruments, an additional set of RT calculations was carried out using the ARM radar–lidar combination but ''removing'' all clouds below 1.5-km height in the calculations (this test will be referred to as ARM NLC, which stands for no low clouds). This should be considered as an extreme, as *CloudSat–CALIPSO* instruments do detect some of the low-level clouds there. To approximate the radiative effects associated with the underreporting of high clouds by the ground-based measurements, we will also compare the *CloudSat* 2B-FLXHR with the *CloudSat–CALIPSO* 2B-FLXHR-lidar radiative fluxes and heating rates (as also done in Haladay and Stephens 2009; Su et al. 2009; Henderson et al. 2013). Again, this should be considered as an amplified signature, as the MPL lidar does detect more clouds than *CloudSat* or MMCR alone (Fig. 1). We note also that the 2B-FLXHR-lidar also adds some amount of low clouds with respect to 2B-FLXHR thanks to *CALIPSO* (see Fig. 1b; L'Ecuyer et al. 2008; Haladay and Stephens 2009; Henderson et al. 2013).

Calculating the relative proportion of radiative flux differences due solely to differences in cloud microphysical retrievals used in the ground-based and satellite products is not a simple task. Besides, RT model assumptions about cloud optical properties are also expected to play a role in those differences. However, the ice cloud retrieval techniques used for 2C-ICE-FLUX (2C-ICE; Deng et al. 2010) and ARM (VarCloud; Delanoë and Hogan 2008) were found to agree reasonably well with in situ microphysics in midlatitude cirrus clouds (Deng et al. 2013), despite different assumptions and approaches. The differences in radiative effects due to different ice microphysics will therefore be roughly characterized by comparing the 2C-ICE-FLUX and 2B-FLXHR-lidar products. Using only the satellite products is indeed a powerful way of overcoming the problem of detecting high clouds from the ground.

a. Comparison of SFC downwelling fluxes

Figure 6a shows the comparison of the PDFs of SFC SW downwelling fluxes as derived from ARM RT at ground and from the two satellite products (2B-FLXHR-lidar and 2C-ICE-FLUX). The median SFC downwelling fluxes are also reported in Table 2. The median fluxes are used instead of mean fluxes given the high skewness of the distributions. However, it is to be noted that differences between PDFs as characterized by median and mean fluxes were found to be very similar throughout. The two satellite estimates of the SFC SW flux PDF are in good agreement (Fig. 6a), which is also seen in Table 2 (median values to within $4\,W\,m^{-2}$). This indicates that potential differences in microphysical retrievals used in the two products do not change the estimate of the SFC SW downwelling fluxes much. The ground-based ARM RT PDF, in contrast, is quite different from the satellite PDFs, with a larger frequency of occurrence of fluxes ranging from 550 to $700\,W\,m^{-2}$ and a lower occurrence of fluxes between 850 and $950\,W\,m^{-2}$, resulting in a median downwelling SW flux of $768\,W\,m^{-2}$ (Fig. 6a), much lower than the satellite estimates (808 and $812\,W\,m^{-2}$). This cannot be attributed to clear-air differences between products, as it was shown in section 2c that the ARM RT product was actually characterized by larger fluxes than the satellite products. The ground-based ARM RT PDF is in much better agreement with RADFLUX than the satellite PDFs. In particular, the larger occurrence of fluxes ranging from 550 to $700\,W\,m^{-2}$ in ARM RT is also observed in RADFLUX. The resulting median SFC downwelling SW from RADFLUX is $748\,W\,m^{-2}$. Thus, ARM RT moderately overestimates (by $20\,W\,m^{-2}$) while the satellite products largely overestimate (by $60–64\,W\,m^{-2}$) the median SFC downwelling SW flux. This overestimation by the satellite products is consistent with the underreporting of low-level clouds below 1.5 km (section 3, Fig. 1), which would tend to allow more SW radiation to reach the ground surface (low-level water clouds have a strong negative cloud radiative effect in the SW). To study that hypothesis further, the ARM RT and ARM NLC (replacing all clouds by clear-air in radiative transfer calculations below 1.5 km height; see introduction to section 4) PDFs are compared in Fig. 7a. Small differences are found for fluxes larger than $600\,W\,m^{-2}$, so the underreporting of the low-level clouds is not responsible for that dip in the PDF between 550 and $700\,W\,m^{-2}$. The investigation of individual cloud scenes producing SW fluxes in that range indicates that such fluxes are produced almost exclusively by low-level cumulus cloud scenes, with the addition of some shallow precipitating cloud cases (tops lower than 3 km) during the wet season. The observed differences are therefore likely mainly due to differences in estimated cumulus frequency of occurrence and retrieved cumulus microphysical properties. This is consistent with results from sensitivity tests conducted in Henderson et al. (2013), which indicate that large global overestimates of 2B-FLXHR-lidar SFC downwelling fluxes can be primarily produced by LWC

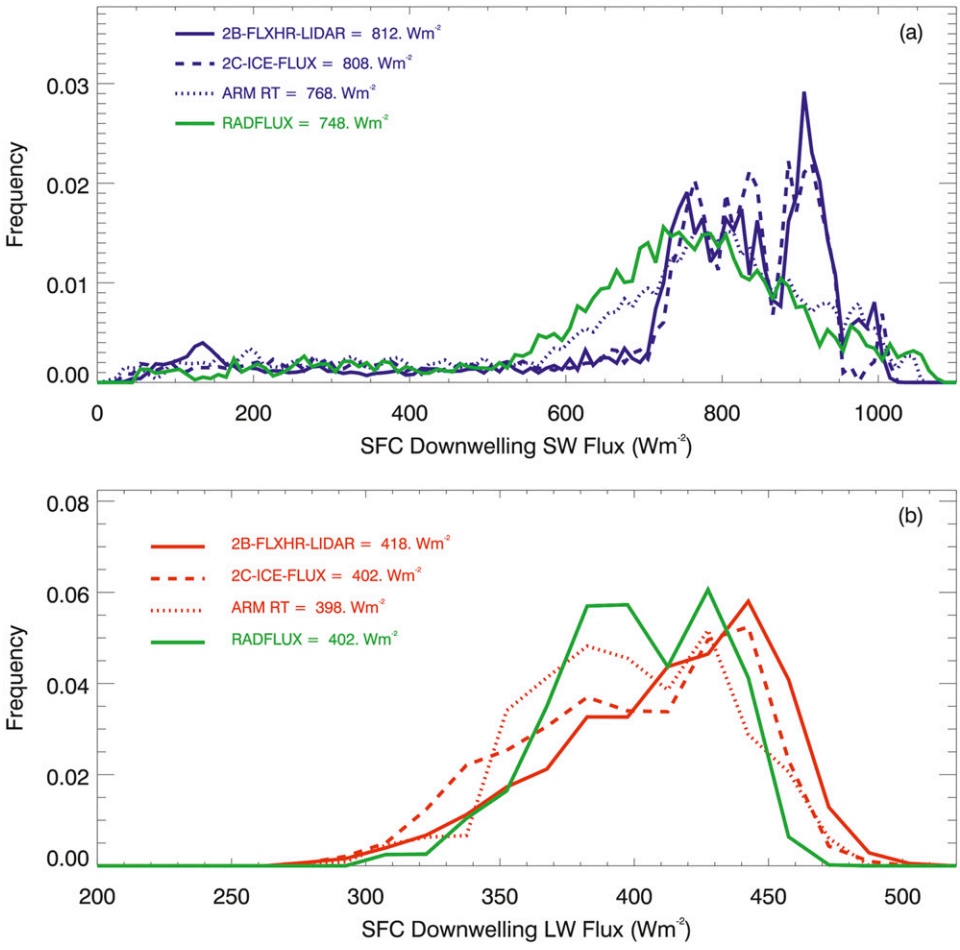

FIG. 6. Comparison of PDFs of the SFC (a) SW and (b) LW downwelling fluxes. The green line shows the reference RADFLUX product. Blue (SW) and red (LW) lines show the 2B-FLXHR-lidar (solid), 2C-ICE-FLUX (dashed), and ARM RT (dotted) products. The median SW and LW fluxes from each product are also listed.

or IWC being too small (a global overestimate of 5.5 and 3.7 $W m^{-2}$ can be produced with underestimates of LWC by 50% and of IWC by 70%, respectively) and cloud base (top) being too high (low) (global overestimate of about 3 $W m^{-2}$ can be produced by an error of 240 m in cloud boundaries).

Let us now turn to the analysis of differences in the SFC downwelling LW flux PDFs (Fig. 6b). The comparison of the 2B-FLXHR-lidar and 2C-ICE-FLUX products seems to indicate this time that the microphysical differences between the two satellite products play a larger role in the LW than in the SW. The 2B-FLXHR-lidar product is characterized by a larger frequency of occurrence of SFC downwelling fluxes ranging from 440 to 510 $W m^{-2}$ than all the other products, while it is characterized by lower occurrence of the LW fluxes ranging from 350 to 400 $W m^{-2}$. The resulting median SFC downwelling LW flux is 418 $W m^{-2}$ for 2B-FLXHR-lidar (Fig. 6b, Table 2), 16 $W m^{-2}$ higher than the reference RADFLUX. In contrast, the 2C-ICE-FLUX and ARM RT estimates are in good agreement with RADFLUX (perfect for 2C-ICE-FLUX, slight underestimation of 4 $W m^{-2}$ for ARM RT). This good performance of the ground-based SFC downwelling LW flux estimates highlights the minimal impact of the underreported cirrus clouds above 10-km height (section 3) on SFC

TABLE 2. Comparison of median SFC downwelling fluxes ($W m^{-2}$) with the reference RADFLUX product. The numbers in parentheses are the differences (product minus RADFLUX).

	SW ($W m^{-2}$)	LW ($W m^{-2}$)	Net ($W m^{-2}$)
RADFLUX	748	402	1150
2B-FLXHR-lidar	812 (+64)	418 (+16)	1230 (+80)
2C-ICE-FLUX	808 (+60)	402 (+00)	1210 (+60)
ARM	768 (+20)	398 (−04)	1166 (+16)

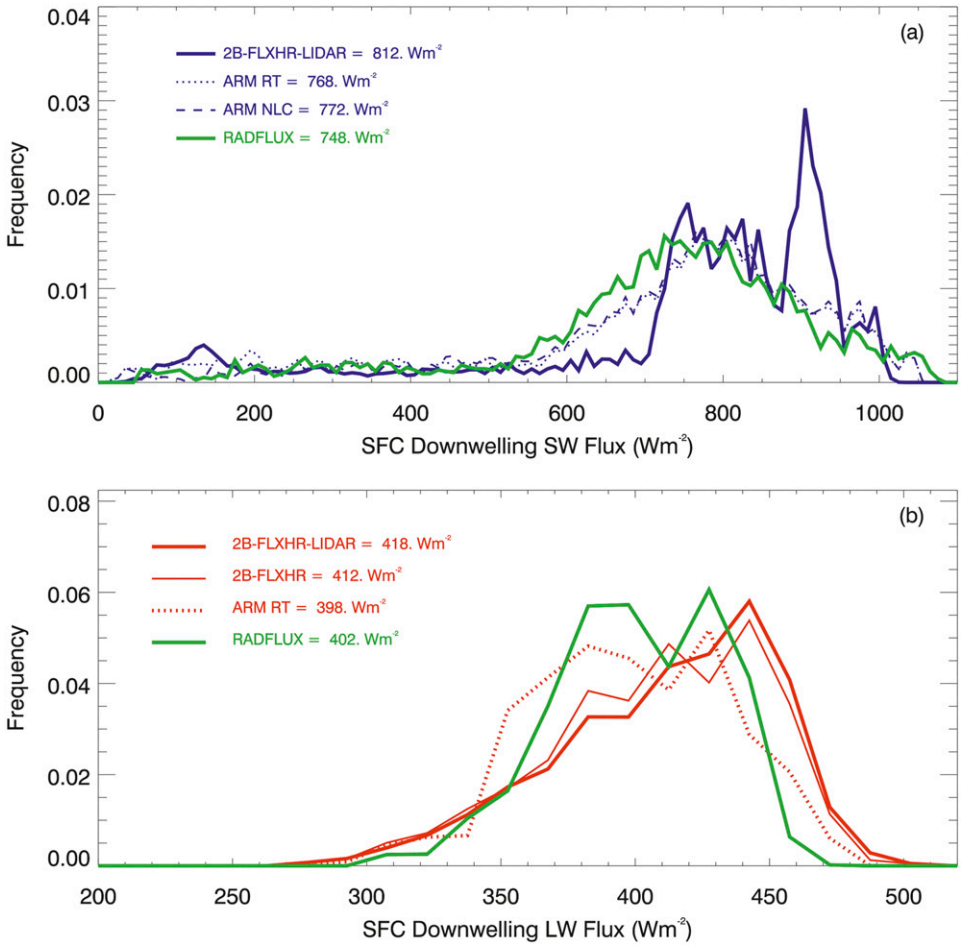

FIG. 7. As in Fig. 6, but for the following products: 2B-FLXHR-lidar (thick solid), ARM RT (thick dotted), 2B-FLXHR [thin red solid in (b)], and ARM NLC [thin blue dashed in (a)].

LW radiation [as also documented in, e.g., McFarlane et al. (2013) locally and Henderson et al. (2013) globally]. This is also confirmed by comparing the 2B-FLXHR and 2B-FLXHR-lidar in Fig. 7b, showing a modest impact of these thin cirrus clouds on the SFC downwelling LW PDF.

In Fig. 6b, it is observed that all products tend to overestimate the occurrence of fluxes larger than 450 $W m^{-2}$, slightly for 2C-ICE-FLUX and ARM RT, but more significantly for 2B-FLXHR-lidar. The investigation of individual cloud scenes producing LW fluxes larger than 450 $W m^{-2}$ in ARM radar–lidar measurements indicates that such fluxes are usually produced by the same cloud scenes responsible for the differences in SW flux PDFs between 600 and 700 $W m^{-2}$ (Fig. 6a): these are low-level cumulus clouds during all seasons, with the addition of some shallow precipitating cloud cases (tops lower than 3 km) during the wet season. Additional cases (about 30% of the cases) are low-level cumulus clouds with an overlying thin or thick cirrus deck. The observed differences are therefore again likely mainly due to differences in estimated cumulus frequency of occurrence and retrieved cumulus microphysics. McFarlane et al. (2013) also show that the LW cloud radiative effect increases with decreasing cloud base height. Therefore, errors in location of the true cloud base in the different satellite products could be another reason for the observed discrepancies, especially in shallow precipitating clouds.

It is out of scope of this paper to further investigate the difference in retrieval techniques that could produce these differences in the SW and LW fluxes. It is, however, suggested that comparisons such as in Fig. 6 should be used to guide further retrieval development work.

b. *Comparison of TOA upwelling fluxes*

Figure 8a shows the comparison of the PDFs of TOA upwelling SW fluxes as derived from ARM RT at

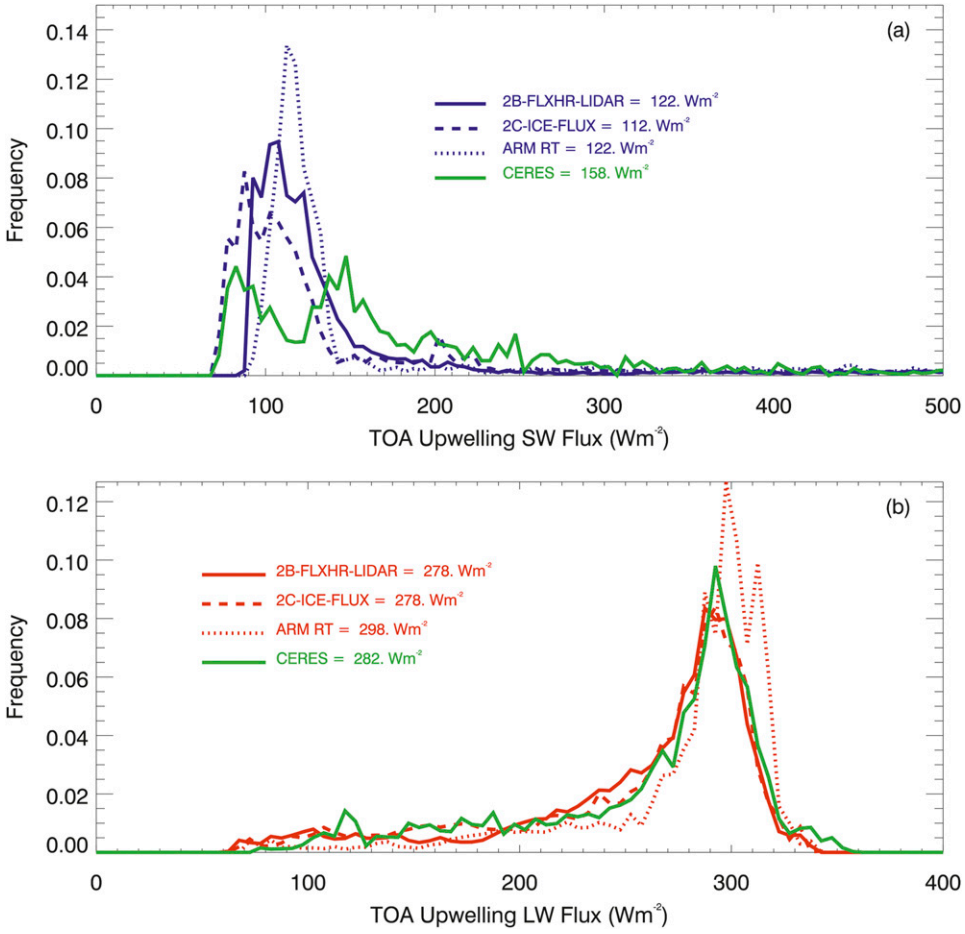

FIG. 8. As in Fig. 5, but for the TOA upwelling fluxes, and the green line is the reference CERES product.

ground level and from the two satellite products. The median TOA upwelling fluxes are also reported in Table 3. From this figure it is clearly seen that all estimates of the PDF of TOA upwelling SW fluxes are very different from the reference CERES PDF. The CERES TOA SW flux PDF is multimodal, with two main peaks centered at 85 and 140 W m^{-2}, while the ground-based ARM RT and the two satellite products are all unimodal, with peaks centered at 110, 100, and 90 W m^{-2}, respectively. The resulting median upwelling SW flux at TOA is largely underestimated by all estimates as well (by 36, 36, and 46 W m^{-2} for ARM RT, 2B-FLXHR-lidar, and 2C-ICE-FLUX, respectively; Table 2). Again, the differences observed between ground-based and satellite products cannot be attributed to clear-air differences as those differences are much larger than the 6 W m^{-2} reported in section 2c. The fact that ARM RT slightly outperforms the two satellite products is somewhat coincidental, as none of the products reproduces at all the functional form of the CERES PDF. The other main general feature is that none of the products is able to generate the CERES frequency of occurrence of SW upwelling fluxes larger than 150 W m^{-2}. Identifying the main reasons for this discrepancy (underreported cloud frequency of occurrence or inaccurate microphysical retrievals) is much more difficult than for the SFC downwelling fluxes, as this comparison of TOA upwelling SW fluxes integrates the complex cloud-downwelling SW radiation interactions all the way down to the SFC, ground–radiation interactions (through surface albedo) at the SFC, and again complex cloud-upwelling SW radiation interactions all the way up to TOA.

TABLE 3. Comparison of median TOA upwelling fluxes (W m^{-2}) with the reference CERES product. The numbers in parentheses are the differences (product minus CERES).

	SW (W m^{-2})	LW (W m^{-2})	Net (W m^{-2})
CERES	158	282	440
2B-FLXHR-lidar	122 (−36)	278 (−04)	400 (−40)
2C-ICE-FLUX	112 (−46)	278 (−04)	390 (−50)
ARM	122 (−36)	298 (+16)	420 (−20)

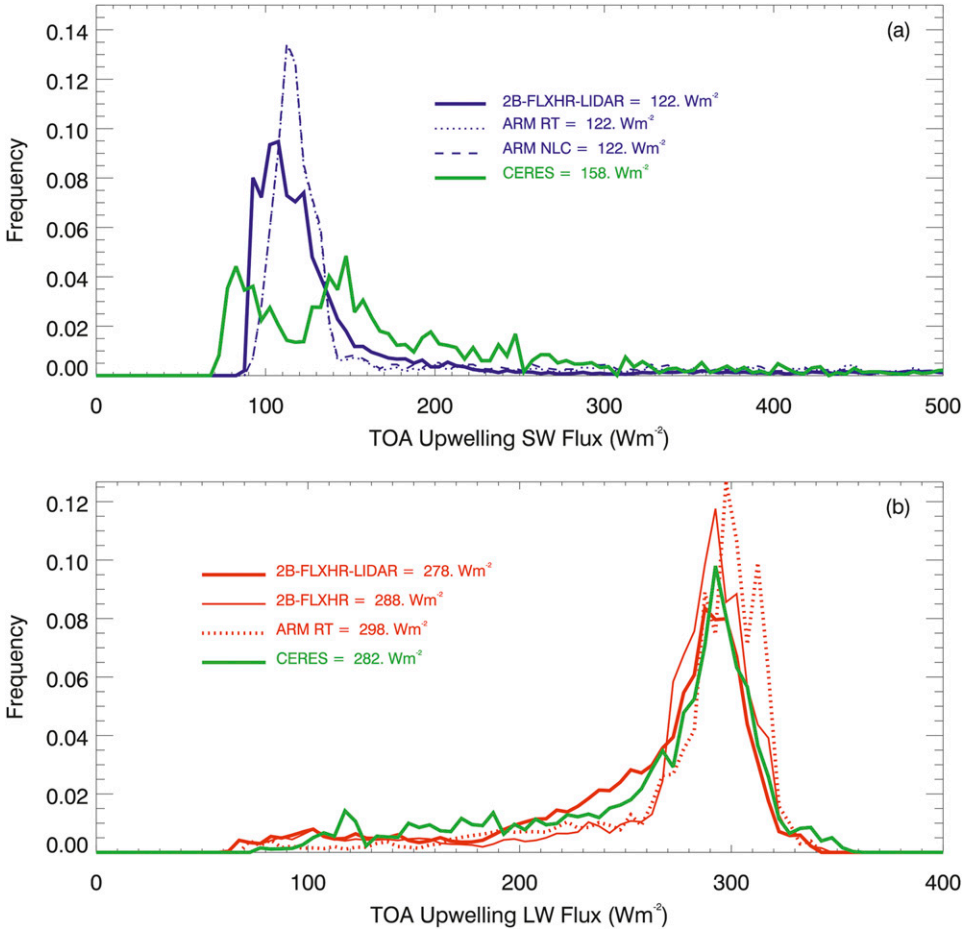

FIG. 9. As in Fig. 8, but for the following products: 2B-FLXHR-lidar (thick solid), ARM RT (thick dotted), 2B-FLXHR (thin solid), and ARM NLC [thin blue dashed in (a)].

The removal of all clouds below 1.5-km height in the ARM RT estimates (ARM NLC) does not produce any difference in the PDF and associated median TOA upwelling SW flux (Fig. 9a), so these clouds underreported by *CloudSat–CALIPSO* do not seem to have a large effect on the TOA upwelling SW fluxes estimated from *CloudSat–CALIPSO*. The very different PDFs in Fig. 8a and the bimodal nature of the CERES PDF suggest that there might be some effect due to land–ocean variability and associated different surface albedos. By splitting our satellite dataset into ocean pixels (Fig. 10a) and land pixels (Fig. 10b), it appears clearly that the first peak at 80 $W m^{-2}$ in the CERES PDF of Fig. 8a is associated with clouds over the ocean, while the second main peak at about 140 $W m^{-2}$ is associated with land-based clouds. We note that this same land–ocean splitting exercise does not yield much change in the SW and LW SFC downwelling and LW TOA upwelling flux PDFs (not shown). The ground-based ''coastal'' statistics (from ARM RT) appear to be more consistent with the satellite products for land-based pixels. It is interesting to note that for land-based pixels all ground-based and satellite products produce a very similar PDF, translating into median TOA SW fluxes within 10 $W m^{-2}$ from each other, which is, however, not in agreement with the CERES estimates (median flux differences of 60–70 $W m^{-2}$). Again, there is a much larger occurrence of CERES fluxes larger than 150 $W m^{-2}$, which is predominantly found for land-based pixels. As also observed in Fig. 10, the ocean satellite retrievals seem to better match the CERES oceanic PDF than do the land-based satellite retrievals agree with the CERES land-based PDFs. Although we cannot really explore further the possible reasons for the observed differences, this study suggests that differences in TOA SW upwelling fluxes are most likely due to a combination of the radiative effects associated with both the underreported clouds below 1.5-km height and the potential inaccuracy of the low-level cloud microphysical retrievals over land. As discussed in section 2c, different

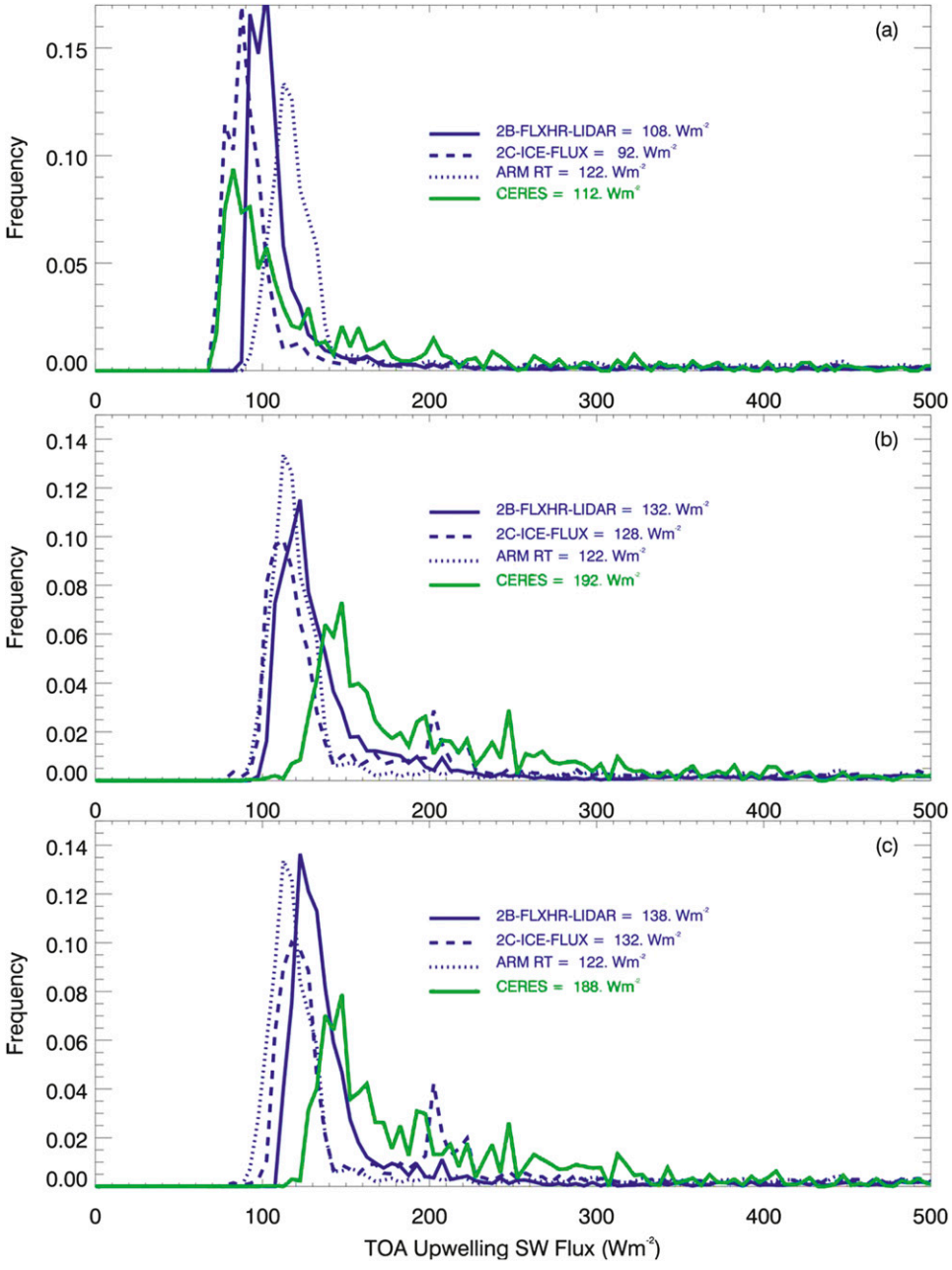

FIG. 10. Comparison of the TOA SW upwelling flux PDFs for satellite (a) ocean pixels, (b) land pixels, and (c) land pixels for which the assumed surface albedo is the same as for the surface ARM RT product. The green lines show the reference CERES product and the blue lines show the 2B-FLXHR-lidar (solid), 2C-ICE-FLUX (dashed), and ARM RT (dotted) products. Note that the ARM RT PDFs are the same in all panels and are given for sake of comparisons only. The median SW fluxes from each product are also given in the panels.

surface albedo assumptions are made in the ground-based and satellite radiative flux calculations, with 47% of the profiles where the same albedo is used (0.095) and 50% where the satellite albedos are lower (0.07). Figure 10c shows a $10\,W\,m^{-2}$ improvement in the agreement between 2B-FLXHR-lidar and CERES median downwelling SFC fluxes ($8\,W\,m^{-2}$ improvement for 2C-ICE) when only the 47% of satellite profiles that use the same albedo are included in the statistics. However, there are still very large differences that cannot be explained by differences in surface albedo assumptions.

From the sensitivity tests conducted in Henderson et al. (2013), underestimates of TOA SW upwelling fluxes can be produced by LWC or IWC being too low,

cloud base being too high, or cloud top being too low. So the same errors in cloud microphysics and cloud boundaries could qualitatively explain both the overestimates of SFC downwelling SW observed in section 4a and the underestimates of TOA upwelling SW discussed just above. Overall, this result clearly illustrates that a lot of work remains to be done in order to reconcile TOA SW upwelling flux measurements with estimates of that same quantity using cloud microphysical retrievals, surface characteristics, and RT modeling. Some of these differences could be due to the fact that radar reflectivity is only relatively weakly dependent on low-level cloud properties in the presence of drizzle-sized droplets, resulting in inaccurate retrievals. We suggest that future work on these aspects should be guided by the type of comparisons presented in our work.

We now turn to the upwelling LW flux comparisons at TOA (Fig. 8b). The two satellite retrievals exhibit quite an outstanding agreement both in terms of reproducing the functional form of the CERES PDF (Fig. 8b) and the median upwelling flux at TOA (slight underestimation of 4 $W m^{-2}$; see Table 3). In contrast, the ground-based ARM RT estimates are clearly biased high, with an overestimation of the median upwelling flux at TOA by 16 $W m^{-2}$ (Table 3). This cannot be attributed to clear-air differences between products as it was shown in section 2c that the ARM RT upwelling LW fluxes at TOA were only 4 $W m^{-2}$ larger than the satellite ones for clear-air profiles. This overestimation results from much lower occurrences of LW fluxes ranging from 190 to 270 $W m^{-2}$ and larger occurrences of fluxes larger than 300 $W m^{-2}$ (Fig. 8b). The obvious hypothesis for this overestimation is the underreporting of a large number of cloudy bins above 10-km height, as shown in Fig. 1 and discussed in section 3. This is confirmed in the sensitivity tests in which 2B-FLXHR and 2B-FLXHR-lidar PDFs of TOA upwelling LW fluxes are compared (Fig. 9b), with the frequency of occurrence of upwelling LW fluxes estimated by 2B-FLXHR dropping in the same flux interval (190–270 $W m^{-2}$) as for ARM RT. This shows unambiguously that this overestimation of the ARM RT upwelling LW fluxes at TOA is largely due to the underreported cirrus above 10-km height. The maximum effect on the median TOA upwelling LW flux with this sensitivity test is 10 $W m^{-2}$, which is not quite as large as the observed difference between ARM RT and CERES (16 $W m^{-2}$), although adding the clear-air differences of 4 $W m^{-2}$ discussed in section 2c would bring it very close. It is also observed in Fig. 9b that the frequency of occurrence of LW fluxes larger than 300 $W m^{-2}$ also increases slightly for 2B-FLXHR with respect to 2B-FLXHR-lidar, albeit not as much as on the ARM RT PDF. So there might also be some effect of the ice microphysical retrieval in the observed differences. Haladay and Stephens (2009) found a tropics-wide LW TOA effect of the cirrus undetected by *CloudSat* of 6.5 $W m^{-2}$ (including clear-sky profiles), with instantaneous cloud radiative effect values of up to 25.8 $W m^{-2}$. Our value for Darwin (16 $W m^{-2}$) does fall within this range.

5. Comparison of radiative heating-rate profiles

While the net radiative heating of the atmospheric column represents the radiative heat source in the atmospheric energy budget and needs to be accurately reproduced by atmospheric models, the detailed vertical distribution of radiative heating also needs to be well reproduced in large-scale models, as it exerts a large influence on the local cloud structure and modulates large-scale tropical circulations (e.g., Mather et al. 2007; Stephens and Webster 1984). The observed net radiative heating associated with tropical anvils and cirrus layers is known to play a major role in the thermodynamic stability of the upper troposphere (Ackerman et al. 1988) and inhibition of tropical convection (e.g., Stephens et al. 2004, 2008). In this section our objective is to evaluate to what extent the large differences found between the ground-based and satellite-derived cloud frequency of occurrence (section 3) and resulting SFC and TOA fluxes (section 4) modify the mean vertical profile of radiative heating rate around Darwin. Note again that an unknown part of the differences found are also probably attributable to different RT model assumptions about cloud optical properties in the different products.

Figure 11 shows the mean vertical profiles of all-sky (which means that clear-sky and cloudy-sky scenes are included here) radiative heating rates over the 2 yr of observations considered in this study. As for the radiative fluxes comparisons in section 4, the precipitation profiles are screened out in these comparisons. The SW radiative heating rate around Darwin is largest below the melting layer, with a peak SW radiative heating of 1.2 $K day^{-1}$ occurring at 2-km height over Darwin (Fig. 11a). The SW radiative heating rate then decreases roughly linearly with height. The ground-based and satellite estimates agree on the general shape of the SW radiative heating-rate profile; however, there are distinct layers where differences are quite large. The differences between the two satellite products characterize the role played by different microphysical retrievals in the estimated SW radiative heating rates. In liquid phase (below 4.5–5 km height), the two satellite products are in very good agreement. The main difference observed between

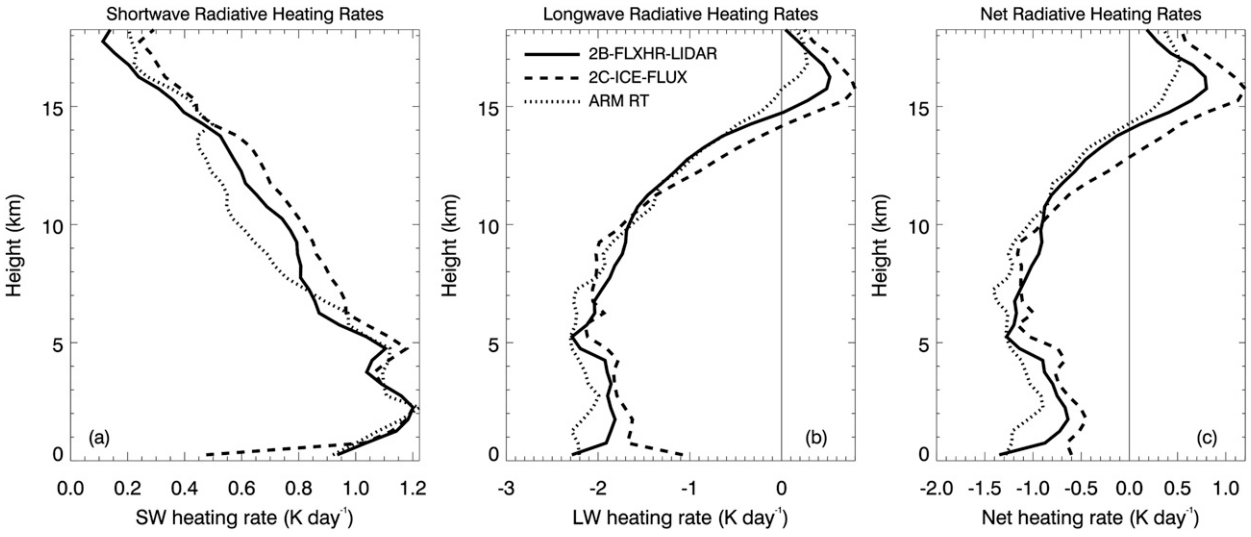

FIG. 11. Mean vertical profiles of (a) SW, (b) LW, and (c) net radiative heating rates derived from the following products: 2B-FLXHR-lidar (solid), 2C-ICE-FLUX (dashed), and ARM-RT (dotted).

2B-FLXHR-lidar and 2C-ICE-FLUX is in the lowest kilometer of the troposphere, where 2C-ICE-FLUX produces a much smaller SW heating than 2B-FLXHR-lidar. The reason for that large difference is unclear. Above the melting layer, 2C-ICE-FLUX exhibits larger SW radiative heating rates, by about 0.1–0.15 K day^{-1} depending on height. This is probably related to differences in the ice cloud microphysical retrievals. The 2C-ICE-FLUX uses a state-of-the-art radar–lidar retrieval technique (Deng et al. 2010) while 2B-FLXHR-lidar uses a radar-only retrieval (2B-CWC) that has been found to be characterized by biases in ice water content and extinction over Darwin (Protat et al. 2010a). In Deng et al. (2013), large high biases in the 2B-CWC cirrus effective radius on the order of a 50%–100% are also found in comparison with aircraft and other retrieval results. The ground-based and satellite estimates of SW radiative heating rates are found to be in good agreement below the melting layer and up to 7-km height, while much smaller SW heating rates are produced by ARM RT from 7- to 14-km height, and slightly larger above 14-km height. Differences between ARM RT and 2C-ICE-FLUX are found to be as large as 0.35 K day^{-1} at 10-km height. This reduced heating in the 7–14-km layer and enhanced heating (or reduced cooling) above 14 km is reminiscent (but with an opposite sign) of the instantaneous effect of optically thick cirrus clouds, which tend to produce cloud-top cooling and in-cloud heating down to their base (e.g., Mather et al. 2007; McFarlane et al. 2008). However, while it seems likely that the underreporting of cirrus by the ARM observations causes the large differences in heating rates between 8 and 14 km, comparison of the 2B-FLXHR and 2B-FLXHR-lidar results (Fig. 12a) shows that the inclusion of the *CALIPSO*-observed clouds has little impact on the SW heating rates in this region. Therefore, the differences between the ARM RT and 2B-FLXHR results are likely due to microphysical differences. The larger effect of the clouds underreported by *CloudSat* on the SW radiative heating is actually found below the melting layer, where the small amount of additional liquid clouds detected by CALIOP only at these heights (see Fig. 1b) produce an additional warming effect of about 0.2 K day^{-1} at all heights.

We now turn to the analysis of the differences obtained for the LW radiative heating rates. Figure 11b shows that the general shape of the vertical profile of LW radiative heating rate is similar in the three estimates, with maximum LW cooling in the midtroposphere. The differences in ice cloud microphysics between 2B-FLXHR-lidar and 2C-ICE-FLUX mainly have an impact on the LW heating above 10-km height, resulting in a reduced LW cooling and enhanced LW warming in 2C-ICE-FLUX when compared with 2B-FLXHR-lidar by about 0.3–0.4 K day^{-1}. Above 10-km height, the impact of the underreported cirrus clouds by the ARM MPL lidar is clearly observed as a reduced warming or enhanced cooling (Fig. 11b). This is also confirmed in the sensitivity test presented in Fig. 12b, where the underreported cirrus clouds by *CloudSat* produce an upper-level cooling bias similar to ARM RT, albeit with an even larger bias, which is expected since the ARM MPL does detect some thin cirrus that *CloudSat* does not detect (Fig. 1). The underestimation of LW radiative warming due to the underreported high clouds in ARM RT ranges from 0.4 (when compared

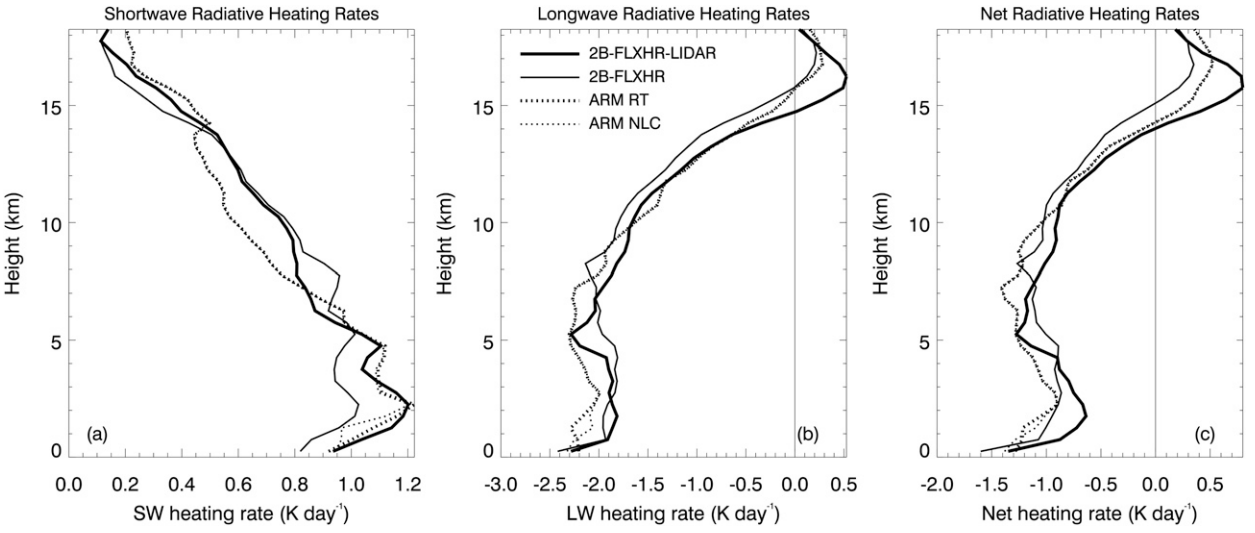

FIG. 12. As in Fig. 11, but with the following products: 2B-FLXHR-lidar (thick solid), 2B-FLXHR (thin solid), ARM RT (thick dotted), and ARM NLC (thin dotted).

with 2B-FLXHR-lidar) to 0.8 K day^{-1} (when compared with 2C-ICE-FLUX), which is very large considering that the heating and cooling rates are of that same magnitude as well. It is important to emphasize here that the differences in satellite estimates of the LW heating rates are of the same magnitude as the difference between ground-based and satellite estimates. The differences due to the underreported cirrus at the ARM site are similar to values reported in Su et al. (2009), who found that tropical cirrus missed by *CloudSat* have a tropics-wide mean heating rate of 0.35 K day^{-1} at 200 hPa.

Overall, the differences in net heating-rate profiles (Fig. 11c) are dominated by the signatures discussed for the LW heating rates (Fig. 11b), with a general enhancement of the differences due to the additional SW biases, especially in the upper troposphere. One important thing to note, though, on the net heating-rate profiles (Fig. 11c) is that the height of zero net heating in the upper troposphere is raised by about 1 km on the ARM RT profile and 2B-FLXHR-lidar profiles when compared with the 2C-ICE-FLUX profile. This height of zero heating is known as a potentially important level (e.g., Gettelman et al. 2004; Fueglistaler and Fu 2006) as it marks the transition from the moist convectively driven Hadley circulation in the troposphere to the wave-driven circulation in the stratosphere. As thin high cirrus microphysics and frequency of occurrence have a large impact on the LW heating rates at these heights (Fig. 11b), they will modulate the altitude of that zero net heating rate and thereby the mass transport from the troposphere to the stratosphere (e.g., Hartmann et al. 2001; Corti et al. 2005).

6. Summary and conclusions

In this paper, 2 yr of collocated ground-based and satellite estimates of the hydrometeor frequency of occurrence and radiative fluxes around the Darwin ARM site are used to establish to what extent these estimates agree. The general conclusion of this study is that current state-of-the-art ground-based and satellite estimates of the cloud frequency of occurrence, downwelling fluxes at SFC, upwelling fluxes at TOA, and mean profile of radiative heating rate cannot be fully reconciled over Darwin. This clearly implies that, although these observations can be used to evaluate the representation of clouds and cloud–radiation interactions in large-scale models, caution should be exercised when doing so, and the limitations of each set of instrumentation should be considered when interpreting model–observations differences.

We first identify in this study that the ground-based radar–lidar combination at the Darwin ARM site does not detect most of the thin cirrus clouds above 10-km height because of instrument limitations and obscuration by lower clouds, and the *CloudSat–CALIPSO* combination underreports the hydrometeor frequency of occurrence below 1.5-m height because of instrument limitations and obscuration by opaque clouds above this height. The underreporting of cirrus by the ground-based instruments is significant because of the frequent occurrence of these cloud types in the tropics (mean frequency of occurrence of about 40% at 15-km height and a high cloud cover above 8 km of 61%, according to the *CloudSat–CALIPSO* radar–lidar estimate). Although the underreporting is less severe with the new

Raman lidar recently deployed at the Darwin ARM site (57% of the satellite-detected cirrus clouds are detected at 15 km with the Raman lidar), the obscuration by low-level clouds is responsible for most of the remaining underreporting of cirrus clouds. Therefore, not much more can be done to improve the cirrus detection from the ground in regions with frequent low cloud cover. It is advised that the statistics of the cloud frequency of occurrence derived from *CloudSat–CALIPSO* should be those used as the reference rather than the ARM statistics above 1.5-km height for such regions, or that conditional sampling is used to screen out the occurrence of low-level obscuration of the ground-based Raman lidar signal.

The radiative impact of these differences (and to an unknown extent of the different RT model assumptions about cloud optical properties) in hydrometeor frequency of occurrence and the resulting cloud radiative forcing is found to be quite large overall. A large overestimation (60–64 $W m^{-2}$) of SFC downwelling SW is found in the *CloudSat–CALIPSO* products when compared with SFC (RADFLUX) reference measurements. These satellite biases are due to both inaccurate low-level cumulus cloud microphysics (although both satellite products agree with each other) and degraded detection below 1.5 km. Therefore, care should be taken when using the *CloudSat–CALIPSO* low-cloud products for model evaluation of cumulus cloud microphysics or surface SW fluxes. Differences between ARM estimates and RADFLUX are much smaller (overestimation of about 20 $W m^{-2}$). In contrast there is a good agreement for the SFC downwelling LW fluxes from both satellite and ground-based retrievals. A 16 $W m^{-2}$ overestimation in SFC LW downwelling fluxes for 2B-FLXHR-lidar, corresponding to an overestimation of the frequency of occurrence of SFC LW fluxes larger than 450 $W m^{-2}$ (also seen but with smaller magnitude in ARM RT and 2C-ICE-FLUX), is due to errors in retrieved low-level cumulus microphysics and/or inaccurate estimates of the true cloud base of shallow precipitating clouds.

The largest and most fundamental differences found in this paper are for the PDF of TOA upwelling SW radiation between ground-based, satellite estimates and CERES measurement, with large median flux biases for all estimates (36, 36, and 46 $W m^{-2}$ for ARM RT, 2B-FLXHR-lidar, and 2C-ICE-FLUX, respectively) and an inaccurate representation of the shape of the CERES PDF. Sensitivity tests indicate that the underreported clouds below 1.5-km height cannot explain all of the bias and that the bimodal structure of the CERES PDF is due to land–ocean differences. The fact that the PDFs are completely different strongly suggests that the microphysical retrievals are responsible for the discrepancies found, especially over land where the differences are largest between satellite retrievals and the CERES measurements. Overall, these results clearly illustrate that a lot of work remains to be done in order to reconcile TOA SW upwelling flux measurements with estimates of that same quantity using cloud microphysical retrievals, surface characteristics, and RT modeling. We suggest that these future efforts should be guided by the type of comparisons presented in this work.

The satellite estimates of the LW upwelling fluxes are in contrast pretty good (slight underestimation of 4 $W m^{-2}$). In contrast, a large overestimation is found for the ARM RT estimate (16 $W m^{-2}$), unambiguously due to the underreported cirrus above 10-km height. These results highlight that great care should be taken when using the ground-based ARM retrievals for climatologies or model evaluation of tropical high clouds.

Although the general shape of the mean vertical profiles of radiative heating rate derived from ground and satellite radar–lidar instruments and RT calculations agree pretty well, large differences are found in some tropospheric layers. SW radiative heating-rate differences are in reasonably good agreement below the melting layer (i.e., associated with liquid clouds). The main differences found in the SW are in ice phase, where the ground-based estimates have much smaller SW heating than the satellite estimates between 7- and 14-km height. Sensitivity tests indicate that this is mostly due to differences in ice microphysics.

Comparisons of the LW heating rates show that the two satellite estimates differ by up to 0.4 $K day^{-1}$ above 12-km height, which is due to the ice microphysics differences. The ground-based LW heating rates are 0.4–0.8 $K day^{-1}$ less than the satellite estimates, which is due to the underreported cirrus above 10-km height at the ARM site in the ground-based retrievals. These differences in LW heating rates are can be considered as large, as they are of the same magnitude as the heating rates themselves.

Acknowledgments. This work was partly supported by the U.S. Department of Energy (DOE) Atmospheric Radiation Measurement (ARM) and Atmospheric System Research (ASR) Programs. The PNNL authors were also partially supported by the NASA Energy and Water Cycle Study (NEWS) program. The Darwin radar, lidar, and radiation data were obtained from the ARM Program Archive (www.arm.gov). The *CloudSat–CALIPSO* data and products were obtained from the *CloudSat* Data Processing Center run by the Cooperative Institute for Research in the Atmosphere (CIRA). *CALIPSO* cloud frequencies in Fig. 3 were

calculated from vertical feature mask data downloaded from the NASA Langley Atmospheric Science Data Center.

REFERENCES

Ackerman, T. P., and G. M. Stokes, 2003: The Atmospheric Radiation Measurement Program. *Phys. Today,* **56,** 38–44.

——, K.-N. Liou, F. P. J. Valero, and L. Pfister, 1988: Heating rates in tropical anvils. *J. Atmos. Sci.,* **45,** 1606–1623.

Austin, R. J., A. J. Heymsfield, and G. L. Stephens, 2009: Retrievals of ice cloud microphysical parameters using the *CloudSat* millimeter wave radar and temperature. *J. Geophys. Res.,* **114,** D00A23, doi:10.1029/2008JD010049.

Battaglia, A., J. Haynes, T. S. L'Ecuyer, and C. Simmer, 2008: Identifying multiple-scattering affected profiles in *CloudSat* observations over the oceans. *J. Geophys. Res.,* **113,** D00A17, doi:10.1029/2008JD009960.

Benedetti, A., G. L. Stephens, and J. M. Haynes, 2003: Ice cloud microphysics retrievals from millimeter radar and visible optical depth using an estimation theory approach. *J. Geophys. Res.,* **108,** 4335, doi:10.1029/2002JD002693.

Bouniol, D., A. Protat, A. Plana-Fattori, M. Giraud, J.-P. Vinson, and N. Grand, 2008: Comparison of airborne and spaceborne 95-GHz radar reflectivity and evaluation of multiple scattering effects in spaceborne measurements. *J. Atmos. Oceanic Technol.,* **25,** 1983–1995.

Campbell, J. R., D. L. Hlavka, E. J. Welton, C. J. Flynn, D. D. Turner, J. D. Spinhirne, V. S. Scott, and I. H. Hwang, 2002: Full-time, eye-safe cloud and aerosol lidar observation at Atmospheric Radiation Measurement Program sites: Instruments and data processing. *J. Atmos. Oceanic Technol.,* **19,** 431–442.

Comstock, J. M., A. Protat, S. McFarlane, J. Delanoë, and M. Deng, 2013: Assessment of uncertainty in cloud radiative forcing and heating rates through retrieval algorithm differences: Analysis using 3 years of ARM data at Darwin, Australia. *J. Geophys. Res. Atmos.,* **118,** doi:10.1002/jgrd.50404.

Corti, T., B. P. Luo, T. Peter, H. Vömel, and Q. Fu, 2005: Mean radiative energy balance and vertical mass fluxes in the equatorial upper troposphere and lower stratosphere. *Geophys. Res. Lett.,* **32,** L06802, doi:10.1029/2004GL021889.

Delanoë, J., and R. J. Hogan, 2008: A variational scheme for retrieving ice cloud properties from combined radar, lidar and infrared radiometer. *J. Geophys. Res.,* **113,** D07204, doi:10.1029/2007JD009000.

Deng, M., G. G. Mace, Z. Wang, and H. Okamoto, 2010: Tropical Composition, Cloud and Climate Coupling Experiment validation for cirrus cloud profiling retrieval using *CloudSat* radar and *CALIPSO* lidar. *J. Geophys. Res.,* **115,** D00J15, doi:10.1029/2009JD013104.

——, ——, ——, and R. P. Lawson, 2013: Evaluation of several A-Train ice cloud retrieval products with in situ measurements collected during the SPARTICUS campaign. *J. Appl. Meteor. Climatol.,* **52,** 1014–1030.

Frisch, A. S., C. W. Fairall, and J. B. Snider, 1995: Measurement of stratus cloud and drizzle parameters in ASTEX with Ka-band Doppler radar and a microwave radiometer. *J. Atmos. Sci.,* **52,** 2788–2799.

Fu, Q., 1996: An accurate parameterization of the solar radiative properties of cirrus clouds for climate models. *J. Climate,* **9,** 2058–2082.

——, and K. N. Liou, 1992: On the correlated *k*-distribution method for radiative transfer in non-homogeneous atmospheres. *J. Atmos. Sci.,* **49,** 2139–2156.

——, P. Yang, and W. B. Sun, 1998: An accurate parameterization of the infrared radiative properties of cirrus clouds for climate models. *J. Climate,* **9,** 2223–2237.

Fueglistaler, S., and Q. Fu, 2006: Impact of clouds on radiative heating rates in the tropical lower stratosphere. *J. Geophys. Res.,* **111,** D23202, doi:10.1029/2006JD007273.

Gettelman, A., P. M. de F. Forster, M. Fujiwara, Q. Fu, H. Vomel, L. K. Gohar, C. Johanson, and M. Ammerman, 2004: Radiation balance of the tropical tropopause layer. *J. Geophys. Res.,* **109,** D07103, doi:10.1029/2003JD004190.

Haladay, T., and G. Stephens, 2009: Characteristics of tropical thin cirrus clouds deduced from joint *CloudSat* and *CALIPSO* observations. *J. Geophys. Res.,* **114,** D00A25, doi:10.1029/2008JD010675.

Hartmann, D. L., J. R. Holton, and Q. Fu, 2001: The heat balance of the tropical tropopause, cirrus, and stratospheric dehydration. *Geophys. Res. Lett.,* **28,** 1969–1972.

Henderson, D., T. L'Ecuyer, G. Stephens, P. Partain, and M. Sekiguchi, 2013: A multisensor perspective on the radiative impacts of clouds and aerosols. *J. Appl. Meteor. Climatol.,* **52,** 853–871.

Illingworth, A. J., and Coauthors, 2007: Cloudnet: Continuous evaluation of cloud profiles in seven operational models using ground-based observations. *Bull. Amer. Meteor. Soc.,* **88,** 883–898.

Im, E., S. L. Durden, and C. Wu, 2006: Cloud Profiling Radar for the *CloudSat* mission. *IEEE Aerosp. Electron. Syst. Mag.,* **20,** 15–18.

Kato, S., T. P. Ackerman, J. H. Mather, and E. E. Clothiaux, 1999: The *k*-distribution method and correlated-*k* approximation for a shortwave radiative transfer model. *J. Quant. Spectrosc. Radiat. Transfer,* **62,** 109–121.

——, G. L. Smith, and H. W. Barker, 2001: Gamma-weighted discrete ordinate two-stream approximation for computation of domain-averaged solar irradiance. *J. Atmos. Sci.,* **58,** 3797–3803.

Kiehl, J., J. Hack, G. B. Bonan, B. A. Boville, D. L. Williamson, and P. J. Rasch, 1998: The National Center for Atmospheric Research Community Climate Model: CCM3. *J. Climate,* **11,** 1131–1149.

L'Ecuyer, T. S., and J. Jiang, 2010: Touring the atmosphere aboard the A-Train. *Phys. Today,* **63,** 36–41.

——, N. B. Wood, T. Haladay, G. L. Stephens, and P. W. Stackhouse Jr., 2008: Impact of clouds on the atmospheric heating based on the R04 *CloudSat* fluxes and heating rates data set. *J. Geophys. Res.,* **113,** D00A15, doi:10.1029/2008JD009951.

Liao, L., and K. Sassen, 1994: Investigation of relationships between Ka-band radar reflectivity and ice and liquid water contents. *Atmos. Res.,* **34,** 231–248.

Loeb, N. G., S. Kato, K. Loukachine, N. Manalo-Smith, and D. R. Doelling, 2007: Angular distribution models for top-of-atmosphere radiative flux estimation from the Clouds and the Earth's Radiant Energy System instrument on the *Terra* satellite. Part II: Validation. *J. Atmos. Oceanic Technol.,* **24,** 564–584.

Long, C. N., 2008: Estimation of upwelling SW and LW for Cape Don and Garden Point using Darwin data. ARM Tech. Data Rep., 15 pp. [Available online at http://iop.archive.arm.gov/arm-iop-file/2006/twp/twp-ice/long-sfcflux/Cape_Don/TWP-ICE_EstUp.pdf.]

——, and T. P. Ackerman, 2000: Identification of clear skies from broadband pyranometer measurements and calculation of downwelling shortwave cloud effects. *J. Geophys. Res.,* **105,** 609–626.

——, and Y. Shi, 2006: The QCRad value added product: Surface radiation measurement quality control testing, including climatologically configurable limits. U.S. Dept. of Energy Tech. Rep. DOE/SC-ARM/TR-074, 69 pp. [Available online at https://www.arm.gov/publications/tech_reports/doe-sc-arm-tr-074.pdf.]

——, and ——, 2008: An automated quality assessment and control algorithm for surface radiation measurements. *Open Atmos. Sci. J.,* **2,** doi:10.2174/1874282300802010023.

——, and S. A. McFarlane, 2012: Quantification of the impact of Nauru Island on ARM measurements. *J. Appl. Meteor. Climatol.,* **51,** 628–636.

Mace, G. G., 2010: Cloud properties and radiative forcing over the maritime storm tracks of the North Atlantic and Southern Ocean as derived from A-Train. *J. Geophys. Res.,* **115,** D10201, doi:10.1029/2009JD012517.

——, R. Marchand, and G. L. Stephens, 2007: Global hydrometeor occurrence as observed by *CloudSat:* Initial observations from summer 2006. *Geophys. Res. Lett.,* **34,** L09808, doi:10.1029/2006GL029017.

——, Q. Zhang, M. Vaughan, R. Marchand, G. Stephens, C. Trepte, and D. Winker, 2009: A description of hydrometeor layer occurrence statistics derived from the first year of merged *Cloudsat* and *CALIPSO* data. *J. Geophys. Res.,* **114,** D00A26, doi:10.1029/2007JD009755.

Marchand, R. T., G. Mace, T. Ackerman, and G. Stephens, 2008: Hydrometeor Detection using *CloudSat*—an Earth-orbiting 94-GHz cloud radar. *J. Atmos. Oceanic Technol.,* **25,** 519–533.

Mather, J. H., S. A. McFarlane, M. A. Miller, and K. L. Johnson, 2007: Cloud properties and associated radiative heating rates in the tropical western Pacific. *J. Geophys. Res.,* **112,** D05201, doi:10.1029/2006JD007555.

Matrosov, S. Y., A. Battaglia, and P. Rodriguez, 2008: Effects of multiple scattering on attenuation-based retrievals of stratiform rainfall from *CloudSat*. *J. Atmos. Oceanic Technol.,* **25,** 2199–2208.

May, P. T., C. Long, and A. Protat, 2012: The diurnal cycle of the boundary layer, convection, clouds, and surface radiation in a coastal monsoon environment (Darwin, Australia). *J. Climate,* **25,** 5309–5326.

McFarlane, S. A., J. H. Mather, T. P. Ackerman, and Z. Liu, 2008: Effect of clouds on the calculated vertical distribution of shortwave absorption in the tropics. *J. Geophys. Res.,* **113,** D18203, doi:10.1029/2008JD009791.

——, C. Long, and J. Flaherty, 2013: A climatology of surface cloud radiative effects at the ARM tropical western Pacific sites. *J. Appl. Meteor. Climatol.,* **52,** 996–1013.

Mlawer, E. J., S. J. Taubman, P. D. Brown, M. J. Iacono, and S. A. Clough, 1997: Radiative transfer for inhomogeneous atmospheres: RRTM, a validated correlated-*k* model for the longwave. *J. Geophys. Res.,* **102,** 16 663–16 682.

Moran, K. P., B. E. Martner, M. J. Post, R. A. Kropfli, D. C. Welsh, and K. B. Widener, 1998: An unattended cloud-profiling radar for use in climate research. *Bull. Amer. Meteor. Soc.,* **79,** 443–455.

Partain, P., 2004: *CloudSat* ECMWF-AUX auxiliary data process description and interface control document. Cooperative Institute For Research in the Atmosphere, Colorado State University, Fort Collins, CO, 8 pp. [Available online at http://www.cloudsat.cira.colostate.edu/ICD/ECMWF-AUX/ECMWF-AUX_PDICD_3.0.pdf.]

Platnick, S., M. D. King, S. A. Ackerman, W. P. Menzel, B. A. Baum, J. C. Riedi, and R. A. Frey, 2003: The MODIS cloud products: Algorithms and examples from *Terra. IEEE Trans. Geosci. Remote Sens.,* **41,** 459–473.

Protat, A., and Coauthors, 2009: Assessment of *CloudSat* reflectivity measurements and ice cloud properties using ground-based and airborne cloud radar observations. *J. Atmos. Oceanic Technol.,* **26,** 1717–1741.

——, J. Delanoë, E. O'Connor, and T. L'Ecuyer, 2010a: The evaluation of *CloudSat* and *CALIPSO* ice microphysical products using ground-based cloud radar and lidar observations. *J. Atmos. Oceanic Technol.,* **27,** 793–810.

——, ——, A. Plana-Fattori, P. T. May, and E. O'Connor, 2010b: The statistical properties of tropical ice clouds generated by the West African and Australian monsoons, from ground-based radar–lidar observations. *Quart. J. Roy. Meteor. Soc.,* **136** (S1), 345–363.

——, ——, P. T. May, J. Haynes, C. Jakob, E. O'Connor, M. Pope, and M. Wheeler, 2011: The variability of tropical ice cloud properties as a function of the large-scale context from ground-based radar-lidar observations over Darwin, Australia. *Atmos. Chem. Phys.,* **11,** 8363–8384.

Slingo, J. M., 1989: A GCM parameterization for the shortwave radiative properties of water clouds. *J. Atmos. Sci.,* **46,** 1419–1427.

Solomon, S., and Coauthors, 2007: Technical summary. *Climate Change 2007: The Physical Science Basis,* S. Solomon et al., Eds., Cambridge University Press, 19–91.

Stephens, G. L., and P. J. Webster, 1984: Cloud decoupling of the surface and planetary radiative budgets. *J. Atmos. Sci.,* **41,** 681–686.

——, and Coauthors, 2002: The *CloudSat* mission and the A-Train: A new dimension of space-based observations of clouds and precipitation. *Bull. Amer. Meteor. Soc.,* **83,** 1771–1790.

——, P. J. Webster, R. H. Johnson, R. Engelen, and T. S. L'Ecuyer, 2004: Observational evidence for the mutual regulation of the tropical hydrological cycle and tropical sea surface temperatures. *J. Climate,* **17,** 2213–2224.

——, S. van den Heever, and L. A. Pakula, 2008: Radiative convective feedback in idealized states of radiative-convective equilibrium. *J. Atmos. Sci.,* **65,** 3899–3916.

Su, H., J. H. Jiang, G. L. Stephens, D. G. Vane, and N. J. Livesey, 2009: Radiative effects of upper tropospheric clouds observed by *Aura* MLS and *CloudSat*. *Geophys. Res. Lett.,* **36,** L09815, doi:10.1029/2009GL037173.

Tanelli, S., S. L. Durden, E. Im, K. S. Pak, D. G. Reinke, P. Partain, J. M. Haynes, and R. T. Marchand, 2008: *CloudSat*'s Cloud Profiling Radar after 2 years in orbit: Performance, external calibration, and processing. *IEEE Trans. Geosci. Remote Sens.,* **46,** 3560–3573.

Thorsen, T. J., Q. Fu, and J. Comstock, 2011: Comparison of the *CALIPSO* satellite and ground-based observations of cirrus clouds at the ARM TWP sites. *J. Geophys. Res.,* **116,** D21203, doi:10.1029/2011JD015970.

Toon, O. B., C. P. McKay, T. P. Ackerman, and K. Santhanam, 1989: Rapid calculation of radiative heating rates and photodissociation rates in inhomogeneous multiple scattering atmospheres. *J. Geophys. Res.,* **94** (D13), 16 287–16 301.

Troyan, D., 2010: Merged sounding value-added product. U.S. Dept. of Energy Rep. DOE/SC-ARM/TR-087, 8 pp. [Available

online at http://www.arm.gov/publications/tech_reports/doe-sc-arm-tr-087.pdf].

Vaughan, M. A., and Coauthors, 2009: Fully automated detection of cloud and aerosol layers in the *CALIPSO* lidar measurements. *J. Atmos. Oceanic Technol.,* **26,** 2034–2050.

Wentz, F. J., and T. Meissner, 2000: AMSR algorithm theoretical basis document (ATBD) version 2: AMSR ocean algorithm. Remote Sensing Systems Tech. Proposal 121599A-1, 12 pp. [Available online at http://eospso.gsfc.nasa.gov/sites/default/files/atbd/atbd-amsr-ocean.pdf.]

Wielicki, B. A., and Coauthors, 1998: Clouds and the Earth's radiant energy system (CERES): Algorithm overview. *IEEE Trans. Geosci. Remote Sens.,* **36,** 1127–1141.

Winker, D. M., and Coauthors, 2009: Overview of the *CALIPSO* mission and CALIOP data processing algorithms. *J. Atmos. Oceanic Technol.,* **26,** 2310–2323.